CLINICAL REFLECTANCE CONFOCAL MICROSCOPE FOR IMAGING OF ORAL CANCER

A Dissertation

by

JOEY JABBOUR

Submitted to the Office of Graduate and Professional Studies of
Texas A&M University
in partial fulfillment of the requirements for the degree of

DOCTOR OF PHILOSOPHY

Chair of Committee,	Kristen. C. Maitland
Co-Chair of Committee,	Javier A. Jo
Committee Members,	Gerard L. Cote
	Philip Hemmer
Head of Department,	Gerard L. Cote

August 2014

Major Subject: Biomedical Engineering

ABSTRACT

Biopsy and histopathology remain the standard method for diagnosis of oral cancer in the clinic today. Early detection of oral cancer is fundamental to a higher survival rate, and a non-invasive method is preferred. This is possible through optical imaging techniques. This dissertation describes the design, development and testing of a clinical reflectance confocal microscope for imaging of oral cancer in combination with macroscopic fluorescence lifetime imaging (FLIM).

A compact bench top reflectance confocal microscope was designed and constructed for use in combination with a bench top FLIM system. The system was evaluated by imaging porcine oral tissue ex vivo and normal and dysplastic hamster cheek pouch tissue in vivo. To facilitate in vivo imaging of the human oral cavity, an electrically tunable lens was integrated in the system for axial scanning and a miniature objective lens was designed and fabricated for access into the oral cavity. Performance of the system was characterized over the full range of axial scanning with the electrically tunable lens. The reflectance confocal microscopy system was tested in combination with macroscopic FLIM by imaging normal and pre-cancerous human oral tissue ex vivo and in vivo in the clinic.

DEDICATION

To my family: my parents Michel and Noelle, my brothers Mitch and Yves and my fiancé Tony.

ACKNOWLEDGEMENTS

Big thanks to my advisor Dr. Kristen C. Maitland, who has guided, helped and supported me; without her, I would not have achieved any of this today.

Big thanks to my co-advisor Dr. Javier A. Jo, who has guided, helped me and always pushed me for the best.

Big thanks to my committee member Dr. Gerard Cote who has generously given me great advice and mentoring me during my Ph.D.

Big thanks to Dr. Philip Hemmer who has always been ready to help me with great feedback and expertise.

Big thanks to all my colleagues at work who have helped this project become successful: Shuna Cheng, Rodrigo Cuenca, Bilal Malik, Meagan Saldua, Cory Olsovsky, Fatemeh Nooshabadi, Astride Tchoffo, and Lee Jordan. Big thanks to Carl Johnson and Steve Zombrano who made the mounts for the pre-clinical and clinical systems.

Big thanks to Texas A&M and the Department of Biomedical Engineering who have showed me a great spirit of inclusion, openness and support.

Big thanks to my parents Michel & Noelle, my brothers Mitch and Yves, and my fiancé Tony who have encouraged me in all steps of my Ph.D.

Big thanks to Jesus, Saint Mary, all Saints including Anthony The Great, Charbel, Nihmatullah, Rafqa, Faustina, Estefan, , Therese de Lisieux, Rita, Anthony de Padua, Jude, Michael, Raphael, and Joseph who have protected and accompanied me during this journey.

NOMENCLATURE

RCM	Reflectance Confocal Microscopy
NIR	Near Infrared
FLIM	Fluorescence Lifetime Imaging
UV	Ultra Violet
FOV	Field of View
USAF	United States Air Force
3D	Three Dimensional
NA	Numerical Aperture
GRIN	Gradient Index
CCD	Charged-Coupled Devices
MEMS	Micro-Electromechanical Systems
GI	Gastrointestinal
OC	Oral Cavity
ETL	Electrically Tunable Focus Lens
PMT	Photomutiplier Tube
MCP-PMT	Micro-channel plate photomultilpier tube
BS	Beam Splitter
APD	Avalanche Photodiode
HWP	Half Wave Plate
QWP	Quarter Wave Plate

NADH	Nicotinamide Adenine Dinucleotide
FAD	Flavin Adenine Dinucleotide
DM	Dichroic Mirror
OL	Objective Lens
IRB	Institutional Review Board
IACUC	Institutional Animal Care and Use Committee
TAMU	Texas A&M University
PBS	Phosphate Buffered Saline
H&E	Hematoxylin and Eosin
DMBA	7; 12-dimethylbenz½α_anthracene
FWHM	Full Width Half Max
N/C	Nuclear to Cytoplasmic
Lt	Length

TABLE OF CONTENTS

Page

LIST OF FIGURES

Page

LIST OF TABLES

Page

CHAPTER I

INTRODUCTION

This dissertation describes the first clinical reflectance confocal microscope that uses a miniature lens with ETL axial scanning. This system has the potential to detect pre-cancer in vivo. This dissertation responds to the following aims:

- Aim 1: to design, construct and validate a compact bench top reflectance confocal microscope to image oral tissue in combination with a bench top FLIM system.
- Aim 2: to design and construct a compact reflectance confocal microscopy system with miniature objective lens for in vivo imaging of the oral cavity.
- Aim 3: to test the capability of reflectance confocal microscopy to image oral tissue ex vivo and in vivo in the clinic.

Chapters in this dissertation are reprinted from journal papers I have first authored. Chapter II is a background summary of oral cancer and optical instrumentation, more specifically confocal endomicroscopy. It reprints parts of: **Jabbour J. M.,** Saldua M. A., Bixler J. N., Maitland K. C., "Confocal Endomicroscopy: Instrumentation and Medical Applications", Annals of Biomedical Engineering, 40(2), p. 378-397, 2012.

Chapter III, which aims to respond to aim 1, describes a multi-scale multi-modal bench top imaging system that uses macroscopic FLIM to find suspicious lesions then uses RCM to image these suspicious lesions with higher resolution. Chapter III validates the use of the combination of the two modalities by imaging ex vivo normal porcine tissue and in vivo normal and dysplastic hamster tissue. Chapter III reprints parts of

Jabbour J. M., Cheng S., Malik B.H., Cuenca R., Jo J.A., Wright J., Cheng Y-S.L., Maitland K. C., "FLIM and reflectance confocal microscopy for multiscale imaging of oral precancer", Journal of Biomedical Optics, 18(4), p. 046012, 2013.

Chapter IV, which aims to respond partly to aim 2, validates the use of ETL in RCM by characterizing its performance and imaging ex vivo human tissue. Chapter IV reprints parts of **Jabbour J.M.,** Malik B.H., Olsovsky C., Cuenca R., Cheng S., Jo J.A., Cheng Y.S.L., Wright J.M., and Maitland K.C., "Optical axial scanning in confocal microscopy using an electrically tunable lens," Biomedical Optics Express, 5(2), 645-652, 2014**.**

Chapter V, which aims to respond partly to aim 2, introduces a new miniature objective design to be used in the RCM system and characterizes it over the axial scan range of the ETL. Chapter V shows new data that is in submission for publication.

Chapter VI, which aims to respond to aim 3, validates the capability of the system by showing ex vivo imaging from normal and abnormal human tissue and in vivo imaging from normal human tissue. Chapter VI shows new data that is in submission for publication.

Chapter VII concludes on the findings of this dissertation and sheds light on future work that needs to be done to continue progression of this project.

CHAPTER II

BACKGROUND*

This chapter is composed of two main parts that aim to provide a background and review to the application and the methods used.

The first part of this chapter comprises of a summary of oral cancer, a short comparison to other type of some epithelial cancers and the motivation behind this work. The chapter also includes a description of morphological and biochemical changes happening with oral pre-cancer progression.

The second part of the chapter is taken from Jabbour J. M., Saldua M. A., Bixler J. N., Maitland K. C., "Confocal Endomicroscopy: Instrumentation and Medical Applications", Annals of Biomedical Engineering, 40(2), p. 378-397, 2012. It comprises of a background on confocal microscopy and a summary of the instrumentation used for various confocal endomicroscopy systems in research as well as commercially available. The summary includes systems used for all kinds of applications, not only for oral cancer. Iot also includes various systems such as rigid confocal endosmicroscopes and flexible confocal endo-microscopes based on fiber optics.

---

* Reprinted with permission from "Confocal endomicroscopy: instrumentation and medical applications" by Jabbour J. M., Saldua M. A., Bixler J. N., Maitland K. C., 2012. *Annals of Biomedical Engineering,* 40(2), p. 378-397, Copyright [2012] by Biomedical Engineering Society.

II.1. Background of oral cancer

Eighty to ninety percent of all cancers originate in epithelial tissues, such as in the OC, cervix, esophagus, and colon. If detected at an early stage, the morbidity and mortality of this disease may be greatly reduced.

Although oral cancer has a relatively low incidence compared to cancers in some other organs as shown in table 1, figure 1 shows that the 5-yr survival rate of oral cancer is worse even when detected locally. Delayed diagnosis is believed to be one of the main causes for the relatively low survival rate. Early detection of premalignant lesions, precursors to cancer, can improve prognosis.

Table 1: Estimated new cases of cancers of prostate, breast and oral cavity.

Site	Estimated New Cases
Prostate	238,590
Breast	234,580
Oral Cavity and Pharynx	41,380

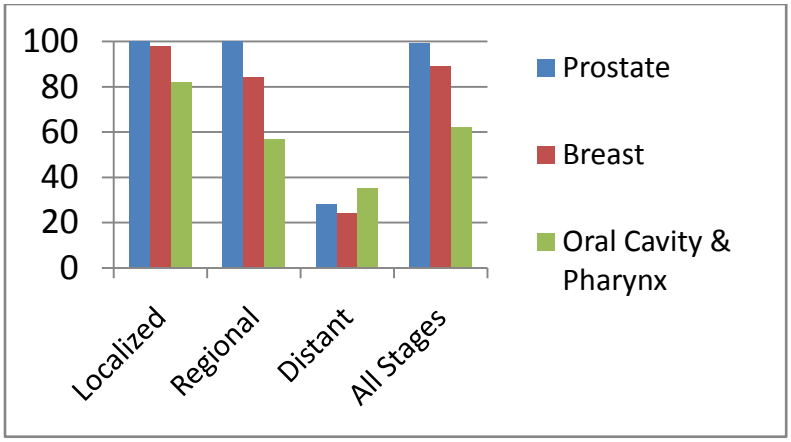

Figure 1: 5-year survival rate of cancers from the oral cavity, breast, and prostate.

Current detection and diagnosis based on clinical visual inspection and palpation by the doctor inside the patient's mouth looking for abnormal lesions; and histopathology evaluation of the biopsy tissue. The biopsy technique is an invasive technique that is expensive, time consuming and susceptible to misdiagnosis due to the heterogeneity of pre-cancer progression. Moreover, histopathology of a biopsy tissue is a study of a non living tissue. There is need to detect pre-cancer non invasively. This could be done using optical imaging techniques, that can detect these changes in vivo enabling evaluation of more locations within the mouth with real-time feedback.. Before description of the optical imaging techniques, description of architectural and biochemical tissue changes associated with pre-cancer progression is described in table 2 and shown in figure 2.

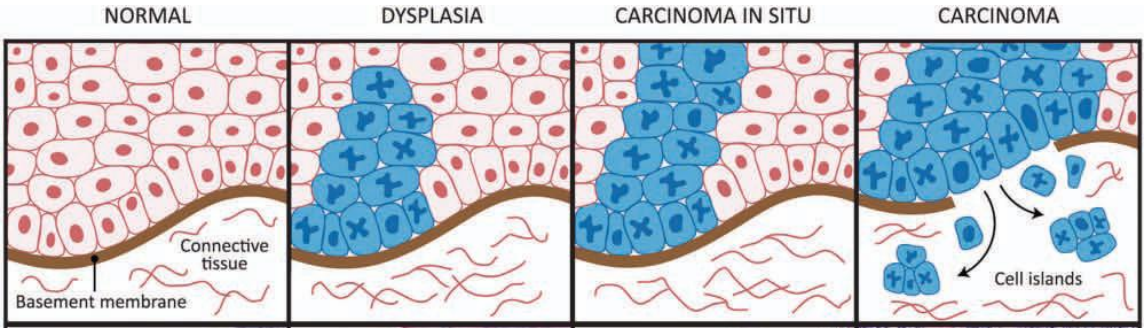

Figure 2: Cartoon showing the progression of pre-cancer between normal and carcinoma state. In a normal sate, no abnormal epithelial cells are seen close to the basement membrane separating the epithelium and connective tissue. In a dysplastic state, the abnormal cells start from the bottom layer of the epithelium and start increasing in number until they fill the full epithelium thickness; at that state, the state of the tissue is called carcinoma in situ. In a carcinoma state, the abnormal cells proliferate to the underlying connective tissue layer and spread to other sites.

Table 2: Changes happening in the epithelium and connective tissue associated with pre-cancer progression.

	Changes Associated with Pre-cancer Progression	
	Biochemical	Architectural
Epithelium	Increase in Metabolic activity	Increase in Nucleus to Cytoplasmic ratio
		Increase in Epithelial thickness
Connective Tissue	Break down of Collagen crosslinks	

The main changes associated with pre-cancer progression can be split into two main parts: the biochemical changes that consist of a breakdown of collagen crosslinks and an increase in epithelial metabolic activity, and the morphological changes that consist of an increase in epithelial nuclear to cytoplasmic ratio and and in crease in epithelial thickness.

The primary endogenous fluorophores of interest in epithelial precancer progression are collagen crosslinks in the stroma and metabolic cofactors NADH and FAD in epithelial cells. Increased cellular metabolism in epithelial dysplasia results in an increase in NADH and FAD fluorescence signal; conversely, in inflammation, the epithelial cell fluorescence decreases slightly [1]. However, the overall tissue fluorescence from abnormal lesions generally decreases due to the more substantial decrease in stromal collagen fluorescence with inflammation and dysplasia. The loss of collagen fluorescence signal is attributed to the breakdown of collagen crosslinks, infiltration of lymphocytes in the stroma, and increased epithelial thickness and scattering [1, 2].

Optical imaging techniques have shown considerable promise towards early detection of pathological changes and are being explored for noninvasive detection of early cancer. Such optical imaging techniques include confocla microscopy, multiphoton imaging, fluorescence lifetime imaging, optical coherence tomography as well as others. We limit our description to confocal microscopy and fluorescence lifetime optical based systems in section 2 of chapters II and to the introduction part of chapter III.

II.2. Confocal endo-microscopy

Scanning confocal microscopy is a well-established optical imaging technique offering significant advantages over conventional wide-field microscopic imaging. In addition to enhanced lateral and axial resolution, the confocal microscope has the ability to image selectively in depth by substantially rejecting out of focus light through the use of a confocal pinhole. This optical sectioning capability enables high resolution imaging of thick biological samples, such as tissue in vivo, without the need for tissue excision, fixation, and sectioning as is required for conventional histological processing.

The confocal microscope was invented by Marvin Minsky in 1955. The Minsky microscope was termed ‘‘confocal’’ because the condenser and OL had the same focal point. A point illumination source is focused into the sample, illuminating a single point at a time. The detection pinhole aperture passes light from the focus, but significantly rejects light from depths in the sample above and below the focal plane as shown in Fig 3(a). To create a two- or three-dimensional image, the sample or the focal spot needs to be scanned laterally and axially. Therefore, high resolution images can be formed from different depths within the sample as shown in Fig. 3(b).

The optical sectioning limit or the axial resolution is primarily dependent on the diameter of the pinhole diameter. The less the diameter of the pinhole is, the better axial sectioning of the confocal system is but less is the collected light. The bigger the diameter of the pinhole is, more reflected light is collected but worse gets the axial resolution. To measure the axial resolution of a confocal microscope, a high reflective surface such a mirror is placed below the objective and scanning axially through the focus of

the objective. Then, the intensity of the light recorded at the detector after the pinhole versus axial steps is plotted, fitted into a Gaussian plot which FWHM would be the measured axial resolution.

Fig.4, that has plots from Wilson and Carlini's [3], helps calculate the theoretical axial resolution of a confocal system. By convolving the point spread function of the lens in the aperture place with the pupil function of the aperture, Fig. 4(b) can be plotted to show the variation of the intensity (I) of the light collected versus dimensionless axial position (u) for different pinhole aperture sizes. Figs. 4(c) and 4(d) show the change of lateral and axial resolution respectively with aperture size change. The first equation in Fig. 4(a) calculates a dimensionless aperture size from the actual pinhole size, wavelength and numerical aperture of objective lens. Once Vp is known, $u_{1/2,}$ half width of the curves in Fig. 4(b), can be deduced from Fig. 4(d) which leads to the calculation of axial resolution Z with second equation shown in Fig.4(a). True confocal operation happens at Vp=0.5 since the resolution stays constant with a Vp smaller than 0.5. Best resolution with maximized sensitivity can still be achieved with Vp<3 since an increase in the pinhole aperture would still have the same resolution in this range.

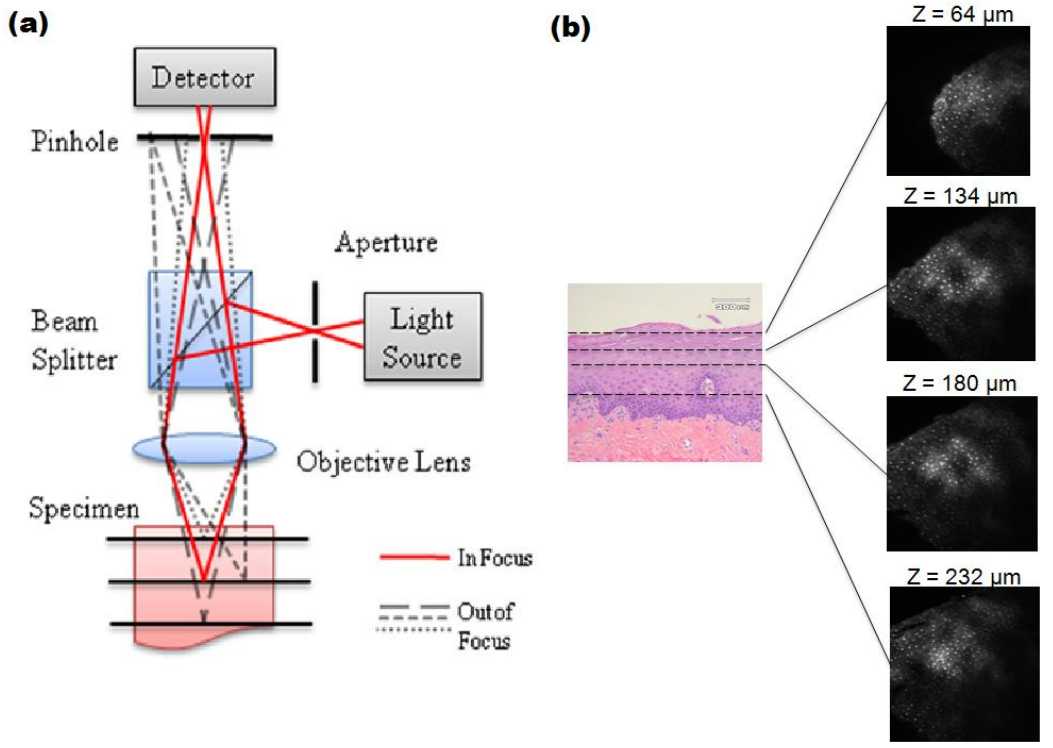

Figure 3: (a) Schematic diagram for confocal microscopy showing rays coming from the focal spot (solid lines) and from out of focus regions above, below, and beside the focal spot (dashed lines). Out of focus rays are rejected by the confocal pinhole. (b) Confocal images from increasing depths of ex vivo normal human oral biopsy tissue with corresponding histology image.

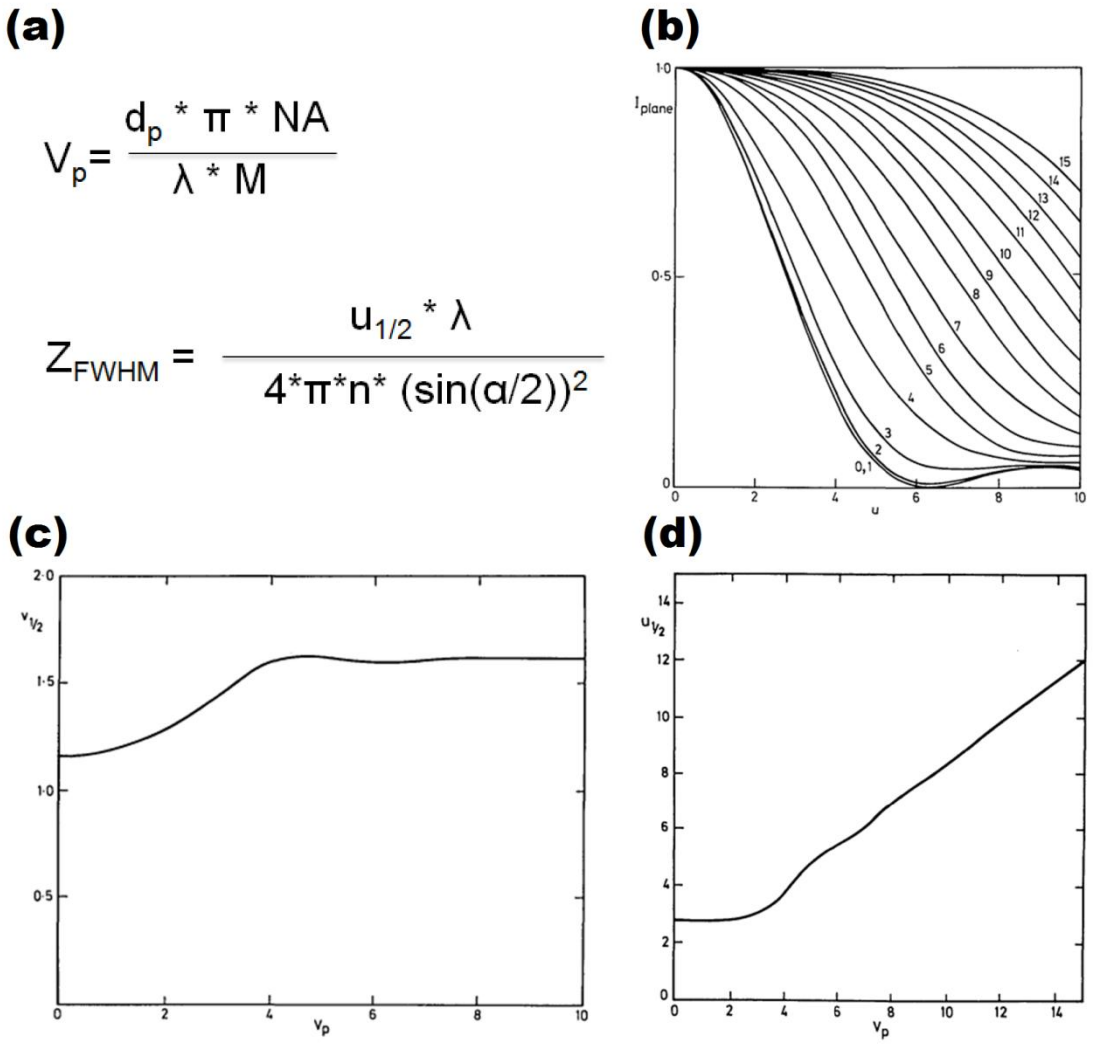

Figure 4: (a) equations of the dimensionless pinhole radius Vp and axial resolution Z in microns calculated from pinhole diameter dp in microns, magnification of the RCM system M, NA or n*sin α of objective lens, refractive index n between objective and sample, and wavelength used λ is the wavelength. (b) variation of intensity against axial position for different pinhole apertures (c) lateral resolution change with change of Vp (d) half width $u_{1/2}$ of the curves in Fig. 4 with change of Vp. [3] Reprinted with permission from "Size of the Detector in Confocal Imaging-Systems" by T. Wilson, and A. R. Carlini, 1987. *Optics Letters*, 12(4), p. 227-229, Copyright [1987] by OSA.

Both fluorescence and reflectance microscopy techniques have been integrated into confocal imaging for a wide array of applications. In particular, confocal microscopy has become a popular tool for high resolution imaging of cells and tissue. In the 1980s and more extensively in the early 1990s, confocal imaging was explored for in vivo imaging of animal and human tissue [4]. Early work was predominantly in accessible organs such as the eye [5, 6], skin [7, 8], and OC [9].

For in vivo imaging, the scanning and image acquisition rate must be sufficiently fast to avoid motion artifacts from a moving subject. In addition to increased imaging speed [10], microscope modifications were made to increase accessibility of the microscope to tissue. For example, in order to image tissue that could not be placed in a traditional confocal microscope, Rajadhyaksha et al. developed a confocal scanning laser microscope with a mechanical arm and rotatable head that allowed for imaging of skin, lip, and tongue in vivo [9]. A ring-and-template assembly was attached to the skin or oral tissue of the subject, which would then mount to the objective housing to minimize motion artifacts. However, the large microscope OL limits this method to in vivo imaging of externally accessible tissue.

A major advance for the translation of confocal microscopy to in vivo clinical imaging was the use of a single mode fiber in place of a traditional confocal pinhole, which has been shown to allow a microscope system to maintain the optical sectioning properties of a traditional confocal imaging system [11]. The use of an optical fiber as the source and detector pinholes allows separation of the imaging arm from the light source and detector, increasing versatility of the confocal microscope for in vivo

imaging . This configuration reduces system complexity and enables automatic alignment of these two confocal apertures [12].

With the implementation of optical fibers to deliver and collect light confocally from tissue, techniques for scanning in vivo and miniaturization of optics and mechanics at the distal end of the light guide encompass much of the technical innovation that has led to clinical endomicroscopy. In general, the scanning techniques can be divided into two modalities: scanning proximally or distally to the light guide. Various methods and technologies have been employed to miniaturize confocal systems so that they can be applied to endoscopic imaging. Although there are tradeoffs between resolution, FOV, and probe size, lateral and axial resolutions down to 0.5 um[13] and 3 um , respectively, FOV as large as 800x450 microns, OL outer diameter down to 350 um [14], and total probe outer diameter down to 1.25 mm[15] have been achieved. The terms ‘‘endomicroscope’’ and ‘‘microendoscope’’ are used interchangeably within the literature. Of the papers referenced here that use either of these two terms, 47% describe the technology as ‘‘endomicroscopy’’ and 63% use ‘‘microendoscopy’’. Therefore, 10% overlap the two groups by using both terms within their text. There has not been a clear distinction between the terms. Here, to remove further ambiguity from the terminology, we define these terms in the context of endoscopy. First, a medical endoscope is a medical instrument that uses optical technology to visualize the inside of the body by passing through body orifices. Illumination and image transmission can be in the form of a long rigid or flexible tube that is able to reach the area of interest inside the body, or images can be wirelessly transmitted via radiofrequency waves to the external

environment in capsule endoscopy. Confocal microscopy inside the body is accomplished using optical fiber technology for illumination and signal collection. Standard endoscopes can have a diameter up to a couple centimeters. An endomicroscope is a microscope that can be introduced inside an endoscope or directly in the body and provides microscopic images of the region of interest. A microendoscope is simply an endoscope that has a very small diameter, a few millimeters or less, that allows access to regions inaccessible to standard endoscopes. However, a microendoscope may not necessarily be a microscope. Several references use ‘‘confocal microendoscopy’’ to describe a miniature endoscope with confocal operation, therefore capable of acquiring microscopic images. We adopt the more precise term ‘‘confocal endomicroscopy’’ for a confocal microscope that can image inside the body.

Confocal endomicroscopes generally fall within two main categories based on proximal or distal scanning and the type of light guide. Proximal scanning at the system side of the light guide is typically achieved through a coherent image guide that relays the scanned pattern to the tissue [16]. The advantage of this technique is that the scanning system is not contained in the endoscopic probe and therefore the size of the scanning system is not limited. However, the resolution is limited by the spacing of the individual fibers within the fiber bundle and the total number of pixels is limited by the number of fibers in the bundle, ranging between 10,000 and 100,000 elements. To avoid this limitation, a single fiber can be used if the scanning technique can be moved to the distal or tissue end of the light guide. Using one or two single mode fibers, various

techniques of distal scanning have been explored to reduce the endoscope size, increase image acquisition speed, and improve image quality. Tables 3 and 4 summarize the specifications for proximal and distal scanning confocal endomicroscopes in the research literature. In addition to describing the research behind confocal endomicroscope instrumentation, we present details on two commercially available confocal endomicroscopy systems, summarized in Table 5.

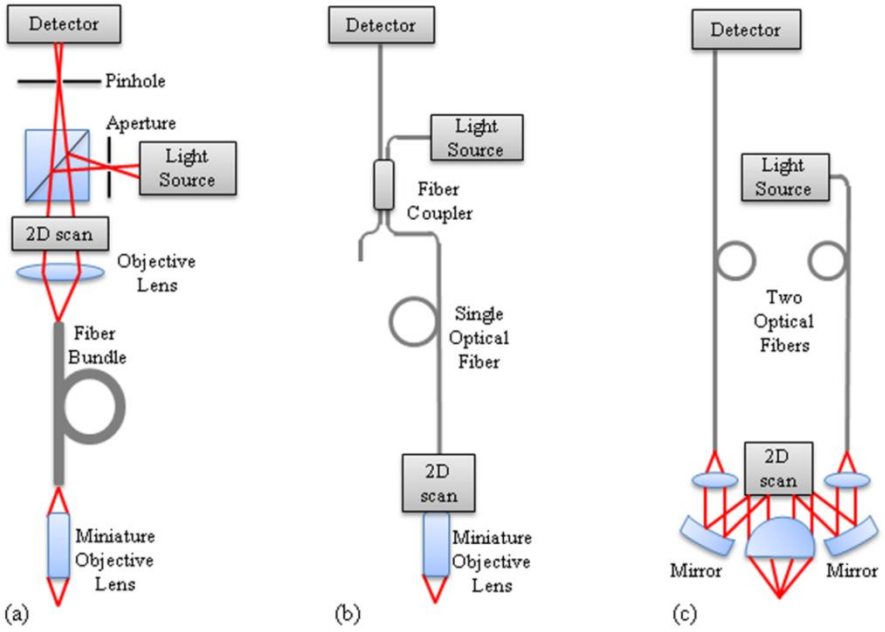

Figure 5: Fiber confocal microendoscope configurations. (a) Proximally scanned microendoscope using a fiber bundle for illumination and detection. The beam is focused to a point and scanned in two dimensions or to a line and scanned in one dimension at the proximal face of the fiber bundle. (b) Distally scanned microendoscope using a single optical fiber for illumination and detection. Scanning can be accomplished by mechanically scanning the fiber, mechanically scanning the fiber and the miniature lens, scanning the beam with a MEMS mirror, or spectrally encoding one axis and mechanically scanning in the second axis. (c) Distally scanned microendoscope using two optical fibers, one for illumination and one for detection, in a dual-axes confocal configuration with a MEMS scanning mirror.

Table 3: Specifications of confocal microendoscope probes with proximal scanning

Reference	Description	Tissue Space NA	Lateral Resolution (µm)	Axial Resolution (µm)	Field of View (µm×µm)
Proximal Scanning					
Knittel et al.	30000 fiber bundle, 2 GRIN lenses, possible application through channel of endoscope, lens: 1 mm dia., 7.8 mm Lt	0.5	3.1	16.6	280 dia.
Lane et al.	30000 fiber bundle, 2 GRIN lenses in 10 mm length of 18 gauge stainless steel tubing, probe inserted in 3.2 mm channel of bronchoscope	0.5	1.4	16-26	230
Kin et al.	30000 fiber bundle, custom objective with 7 lenses, rigid housing: 10 mm dia., 25 mm Lt	0.45	3.3	50	N/A
Tanbakuchi et al.	30000 fiber bundle, custom objective in rigid micro-laparoscope, rigid housing: 5 mm dia., 350 mm Lt	0.46	3	25	450 dia.
Landau et al.	30000 fiber bundle, custom objective with 3 lenses in 18 gauge hypodermic needle	0.4	0.9	N/A	250 dia.
Sung et al.	30000 fiber bundle, custom objective with 8 lenses, rigid housing: 7 mm dia., 22 mm Lt	1	2	10	180 x 170
Kim et al.	No fiber, rigid probe, 3 GRIN lenses and side-viewing prism, rigid housing: 1.25 mm dia., 50 mm Lt	0.45	1	10	250 dia.
Farahati et al.	No fiber, rigid probe, 10 rod relay lenses and a custom objective, rigid housing: 5 mm dia., 230 mm Lt	0.9	1-2	5	400 dia.

Table 4: Specifications of confocal microendoscope probes with distal scanning

Reference	Description	Tissue Space NA	Lateral Resolution (µm)	Axial Resolution (µm)	Field of View (µm×µm)
Distal Scanning					
Giniunas et al.	SF, 11 GRIN rod lenses and a hemisphere lens, lens: 1.5 mm dia., 89 mm Lt	N/A	1.3	30	190 dia.
Pillai et al.	SF, 2 GRIN lenses in 22 gauge hypodermic needle, in 18 gauge guiding needle, lens: 350 µm dia., 27 mm Lt	0.29	0.87	11.5	70 dia.
Dickensheets et al.	SF, 2 MEMS scanners, off-axis phase grating lens, lens and scanner housing: 1.2 mm x 2.5 mm, 6.5 mm Lt	0.24	1	N/A	100 dia.
Kumar et al.	SF, 2-axis MEMS scanner, objective of 2 doublets and a high NA lens, lens and scanner housing: 18 mm dia., 54 mm Lt	0.48	0.5	4.2	200 x 125
Shin et al.	SF, 2-axis MEMS scanner, objective of 2 achromats and an aspheric lens, lens housing: 5 mm dia., 35 mm Lt	0.33	0.83	9.55	140 x 70
Ota et al.	SF, unimorph fiber scanner, aspheric lens, lens and scanner housing: 3.5 mm dia., 30 mm Lt	0.55	1	5.4	90x 150
Piyawattanametha et al.	Dual axis, 2-axis MEMS scanner, 2 parabolic mirrors and a hemisphere lens, lens and scanner housing: 10 mm dia.	0.12	5	7	800 x 450
Pitris et al.	SF, spectrally encoded with dual prism grating, high NA lens, rigid housing: 10 mm dia.	0.9	1.1	N/A	658 dia.

Miniaturization of the scanning optics required for a confocal microscope can be difficult and costly. To overcome this issue, the use of a fiber bundle in place of a single mode fiber has been demonstrated [16]. Optical fiber bundles are flexible light conduits made from tens of thousands of individual step-index fibers. Coherent image guides, in which the arrangement of the fibers is maintained along the length of the bundle, are extensively used in endoscopic imaging using white light illumination and wide-field detection. In addition, optical contrast techniques such as chromoendoscopy, fluorescence endoscopy, and narrow band imaging have been applied to wide-field endoscopy to improve diagnostic capability [17]. In contrast to wide-field endoscopy, confocal endomicroscopy requires scanning of the beam across the face of the fiber bundle to exploit the confocal aperture of the individual optical fibers. Scanning can be accomplished using point scanning, slit scanning, or spatial light modulator techniques. A generalized configuration of proximally scanned confocal endomicroscopy is shown in Fig. 5a. Because the scanning occurs at the system side of the bundle, commercially available scanning optics can be employed. Illumination light is transmitted to the distal end of the bundle where miniaturized optics are needed to focus the light into the tissue, collect the reflected or fluorescent signal, and couple it back into the same fiber. The non-imaging space between fiber cores typically limits resolution and causes pixilation in the images; therefore, image processing is necessary to improve the image quality [18, 19].

The first demonstration of the use of a fiber bundle for confocal imaging was presented by Gmitro and Aziz using a standard Zeiss LSM10 confocal microscope in

fluorescence mode to raster scan a 10,000 element coherent bundle [16]. Although the optical sectioning capability of higher order modes is very similar to that of a single mode, Juskaitis et al. found speckle to be a problem in laser-based reflectance endomicroscopy through a fiber bundle in multimode operation . To address this, incoherent white light illumination was scanned with a Nipkow disc tandem scanning microscope to produce the first real-time reflectance confocal endoscopic images using a 50,000 element bundle. Angle polishing of the fiber bundle and index matching were employed to reduce specular reflection from the proximal end of the fiber, a persistent challenge for reflectance confocal endomicroscopy through a fiber bundle. Collier et al. constructed an entire confocal microscope from commercial optics instead of using an existing confocal microscope. This system was later modified to include custom optics at the proximal and distal ends of the 30,000 element bundle to improve imaging performance and was used to image epithelial tissue [20, 21].

Slit scanning is an alternative fiber bundle scanning technique which uses a line illumination and slit aperture detector instead of a point source and pinhole detector to increase image acquisition speed with a slight sacrifice in axial resolution [22]. Sabharwal et al. demonstrated an innovative slit-scanning fluorescence confocal endomicroscope with a single scanning mirror that scans the line illumination across the bundle, descans the fluorescent light for detection through the fixed slit aperture, then re-scans the spatially filtered signal onto a two-dimensional CCD camera to create real-time confocal images without the need for synchronization [22]. Subsequently, Rouse and Gmitro modified the slit-scan system to demonstrate multi- spectral detection by

incorporating a dispersing prism in the detection arm to collect both spatial and spectral information [23]. Coherent image guides are the pre-dominant type of bundle used for fiber bundle confocal endomicroscopy; however, Lin and Webb exploited the spatial scrambling of an incoherent fiber bundle to convert a slit-scan illumination to a parallel random point scan at the distal tip of the endoscope [24]. The system has the simplicity of the slit-scan confocal endomicroscope and the optical sectioning capability of the point-scan technique. The image of the sample has to be reconstructed based on the random fiber mapping of the bundle.

Other scanning techniques include the use of spatial light modulators. Lane et al. used a digital micromirror device with a high pixel count and fast response to sequentially illuminate individual or multiple fibers within a fiber bundle [25]. Optical sectioning and contrast are improved by only illuminating fiber cores and not the non-imaging space between fibers. Recently, Thompson et al. presented a novel method analogous to adaptive optics to use a spatial light modulator to correct for phase aberrations in the fiber bundle and to additionally add curvature and tip-tilt to the wavefronts to focus and scan the beam at the distal tip of the fiber bundle without optical or mechanical components [26]. While the use of a spatial light modulator was shown to allow 3D imaging, the reported system suffers from a very low frame rate. Acquisition for a single 50 x 50 pixel image was reported to take 15–20 min, with an axial resolution of approximately 100 um and a FOV limited to 80 um diameter.

Although the scanning mechanism does not need to be miniaturized for fiber bundle confocal endomicroscopy, a miniaturized high NA OL is still required to focus

light into tissue and collect reflected or fluorescent signal. The main optical design challenge lies in achieving a doubly telecentric, high NA OL with minimized aberrations and a small outer diameter. GRIN lenses are ideal for their small outer diameter; however, high NA GRIN lenses suffer from optical aberrations. Consequently, GRIN lenses are usually assembled back to back or assembled with other high NA lenses. Custom complex glass lenses have been designed and fabricated for both fluorescence and reflectance confocal endomicroscopes [22, 27-29]. Plastic and combined glass and plastic miniature objectives have demonstrated the potential for inexpensive disposable endomicroscope probes [30-33]. Custom designed lenses have been based on Amici, Petzval, and design by halves design methods [27, 28]. A more cost-effective approach is to start the design with commercial optics and add custom elements to correct aberrations [11, 32]. In order to minimize back reflections, shorten the overall lens length, and reduce the complexity of assembly, a major design goal has been to reduce the number of optical elements in the miniature OLes.

A few endomicroscope specifications dictate the ease of use within the instrument channel of a flexible endoscope. In addition to a small outer diameter, the length of the endomicroscope must be sufficiently flexible and the rigid tip or imaging head of the endomicroscope must be short. While the minimum bending radius for a single optical fiber may be as low as 5 mm, the minimum bending radius for fiber bundles ranges from 10 mm for a 0.25 mm diameter bundle to 200 mm for a 3 mm diameter bundle. The drawback of reducing the bundle outer diameter is the concomitant reduction of the number of fibers in the bundle which corresponds to the number of

pixels in the image. Even if the image guide is sufficiently flexible, the endomicroscope may not be able to be inserted into the instrument channel of a flexible endoscope or navigated through tortuous paths within the body if the rigid imaging head at the distal end of the probe is too long. Table 3 includes dimensions of the rigid sections of various endomicroscopes.

In benchtop confocal microscopic imaging of cellular or tissue samples, it is relatively easy to translate the sample using a translation stage to scan the specimen in the axial direction. Axial scanning is critical for many of the clinical endomicroscopy applications, but is much more challenging at the distal end of a fiber-based probe inside of a living body. Hydraulic, pneumatic, and mechanical scanners have been employed to scan the lens or the tissue. Additionally, optical axial scanning techniques have also been explored, such as the adaptive phase compensation approach [32]. Gmitro and Rouse have optimized a depth scanning technique starting with their original design of a hydraulic focus mechanism in 2001 . While the miniature OL was fixed relative to the position of the tissue, the fiber bundle was scanned by a piston controlled hydraulically. However, this system was not sufficiently compact and was susceptible to fluid leaks and air bubbles. Subsequently, a pneumatic design to control the fiber position relative to the lens was used as a focusing mechanism [28]. In this design, a manual micrometer was used to achieve depth scanning and focus which resulted in slow movement and inherent hysteresis. Therefore, a computer-controlled high speed positioning system that automatically corrected for hysteresis was developed with a positioning accuracy less than the axial resolution [34]. Sung et al. employed hydraulic suction directly on the

tissue to scan the tissue relative to the lens. Due to differences in tissue mechanical properties, hydraulic suction suffers from inaccuracies in positioning and the inability to know exact imaging depth. The possible introduction of air bubbles in the immersion medium is an additional challenge. Lane et al. demonstrated a promising technique to exploit the chromatic aberration of a GRIN lens to spectrally scan the working distance.

Confocal endomicroscopes designed for clinical imaging are commonly flexible endoscopes with a short rigid section at the tip that houses the miniature OL and, in the case of distal scanning endoscopes, the miniature scanning mechanism. Laparascopes or rigid endoscopes have a longer rigid section in the form of a handheld device. A few rigid confocal endomicroscopes have been developed, primarily for preclinical applications, without the use of optical fibers. This is particularly useful for non-linear optical microscopy where the dispersion in the long length of glass in an optical fiber may influence the laser pulse width. These rigid microendoscope designs typically have a small diameter lens system that can be inserted into an animal for intravital imaging. Depending on the imaging depth required, an image relay is commonly used to extend the length of the probe tip. Scanning is performed proximal to the miniature lens system and does not need to be miniaturized due to the location outside of the body. Without any flexibility in the optical system, this configuration is impractical for clinical use. However, a single fiber may be used to deliver the beam to the scanning system and lens and serve as the confocal pinhole. Therefore, these rigid endoscopes potentially span distal scanning and proximal scanning depending on the scanning and fiber system arrangement. Multiphoton and confocal endomicroscopes have been implemented using

GRIN doublets and triplets in a direct view [35-38] or side-viewing probe by adding a prism at the distal tip [15, 39]. In 2010, Farahati et al. developed a rigid confocal endomicroscope using a series of rod lenses with a 0.9 NA miniature OL[40].

Confocal endomicroscopes employing various distal scanning mechanisms typically use one or two optical fibers for illumination and collection of light, illustrated in Figs. 5 b and 5 c, respectively. Kimura and Wilson first proved the use of a single mode fiber for confocal detection in 1991 by replacing the pinhole in a confocal microscope with an optical fiber.[11] Miniaturization of OLes and scanning optics quickly followed in an effort to image inside the body.

Giniunas et al. built and tested a scanning confocal microscope using a single optical fiber for illumination and collection and as the confocal pinhole. Reflected light was coupled back into the laser for sensitive intracavity detection. The optical fiber and single hemisphere lens were fixed together in a scanning probe that was scanned using piezoelectric transducers in a Lissajous scan pattern.

Benschop and Vanrosmalen exploited the two-dimensional scanning of a compact disc player reading head by replacing the laser in the device with a fiber for remote delivery and confocal collection [41].

In 1992, Juskaitis et al. scanned the object in a fiber-based system with intracavity detection. In later work, Juskaitis and Wilson demonstrated the use of a fiber coupler to separate illumination and detection paths, which were scanned synchronously to generate an image [42].

As mentioned in the previous section, some rigid endoscopes that utilize single fibers for their confocal aperture and flexibility employ relatively large scanning systems at the distal end of the optical fiber. A long relay lens, frequently a GRIN lens, is used to offset the imaging field from the bulky scanning [43]. Two-dimensional mechanical scanning of a lensed fiber as an input into a long GRIN relay lens has also been shown to reduce off-axis aberrations that may be imposed by more traditional mirror scanning [14]. Although the scanning mechanism is large, the 350 umm diameter GRIN rigid endomicroscope is mounted in a 22-gauge hypodermic needle to penetrate up to 15 mm into tissue. Other endomicroscopes employ electromagnetic or piezoelectric actuators to distally scan the fiber and OL, which are mounted together [13, 36, 44-46]. This configuration also reduces off-axis aberrations through the single high NA plano-aspherical lens.

Dickensheets and Kino pioneered the field of MEMS based scanners for confocal endomicroscopes. In 1994, they presented the use of a resonant cantilever to scan a single fiber with a Fresnel zone plate miniature OL[47]. Later, the first use of micro-machined silicon scanning mirrors in single fiber endomicroscopy was demonstrated [48, 49]. Two separate micromirrors placed at the distal end of the fiber scan the beam in two dimensions, and a miniature off-axis phase zone plate fabricated by etching fused silica serves as an OL. More recently, Dickensheets has developed a MEMS deformable mirror for focus control and aberration correction, to be integrated into a biomedical endoscope [50, 51]. The main challenges in developing miniaturized scanning mirrors

are to achieve a robust device with large scan angles, large mirror dimensions, and sufficiently fast scanning within a small package.

Murakami at Olympus Optical Co. developed a prototype 3.3-mm diameter confocal endomicroscope to pass through a working channel of an endoscope using a single MEMS electrostatic gimbal scanning mirror and an aspherical OL [52, 53]. Other two-axis scanning mirror designs used in confocal endomicroscopy include an electrostatically driven torsional silicon micromirror with electroplated nickel hinges and frame, a gimbaled scanner using electrostatic combdrive actuators [54-56], and a thermally actuated non-resonant scanner fabricated using silicon-on-insulator multi-user MEMS processes [57]. In addition to micromirrors, other microdevices to mechanically scan the fiber, such as unimorph cantilevers, have also been used for scanning [58]. Integrated optical focusing and mechanical scanning devices have also been fabricated [54, 59].

High resolution confocal endomicroscopes typically require high NA miniature OLes which inherently have a short working distance. Consequently, post-objective beam scanning is impractical within this short working space. To overcome this limitation, Wang et al. introduced a novel optical sectioning technique using a dual-axes geometry [60]. The depth of focus of a low NA lens is too large for adequate optical sectioning in tissue; however, by crossing the axes of two separate illumination and collection beam paths, improved resolution and a long working distance can be achieved with low NA lenses. This enables post-objective scanning [61], which has been accomplished with a biaxial barbell-shaped MEMS scanning mirror [62, 63]. Dual-axes

reflectance and fluorescence confocal endomicroscopy have been implemented using various excitation wavelengths, and engineering improvements continue to reduce the size of the probe head [63, 64].

In vivo endomicroscopic imaging requires fast image acquisition rates, on the order of 10 frames per second or faster, to avoid motion artifacts. High fidelity distal scanning in two dimensions is challenging at these speeds in a compact package. To eliminate one axis of mechanical scanning, Tearney et al. introduced the concept of spectrally encoded confocal microscopy [65]. A broadband source is dispersed laterally by a diffraction grating so that the spatial position is encoded in the wavelength. All wavelengths can be transmitted through a single fiber and the spatial position of the reflected light can be decoded by spectral detection [66]. The second axis of scanning can be performed with a piezo-electric transducer. Image acquisition rates up to 30 frames per second were achieved by using a rapid wavelength swept source [67]. A dual prism grating element was used to miniaturize the probe head [68]. The addition of a motor shaft and linear stage for helical scanning was used to demonstrate large area spectrally encoded confocal imaging of luminal surfaces [69].

Two commercial confocal endomicroscopy systems are currently in use in clinical applications. The Pentax ISC-1000 confocal endomicroscopy system with the EC3870CIK scope (Pentax/Hoya, Tokyo, Japan and Optiscan Pty Ltd, Notting Hill, Victoria, Australia) is a miniaturized Optiscan confocal endomicroscope incorporated into a conventional video-endoscope. The second system approved for clinical use is the Cellvizio (Mauna Kea Technology, Paris, France). The Cellvizio is a standalone imaging

system based on a fibered technology capable of being incorporated into a conventional endoscope [70]. Cellvizio confocal miniprobes can be passed down the accessory channel of any standard endoscope, allowing for rapid image capture in vivo in real time.

Table 5: Commercial confocal microendoscope probes

Probes		Lateral Resolution (µm)	Axial Resolution (µm)	Field of View (µm×µm)	Working Distance (µm)
Optiscan/ Pentax ISC-1000		0.7	7	475×475	250
Mauna Kea Cellvizio	S	5	20	600×500	0
	HD	2-3	20	240×240	30-80
	Z	5	30	600×500	70
	mini O	1	3	240×240	30
	Alve oFlex	5	100	600×500	0

The Optiscan confocal endomicroscope was developed out of the work of Delaney and Harris [71, 72]. The technical specifications of the Optiscan/Pentax ISC-1000 system presented here are summarized from Polglase et al [73]. A distally scanned single optical fiber serves as both the illumination and detection confocal pinholes. The

beam is raster-scanned by scanning the fiber with an electromagnetically driven scanning mechanism. The fiber and lens are contained within the probe and coupled to the sample via an optical window. The window is placed in contact with the tissue to stabilize the probe and to create a reference point for axial scanning. A z-actuator, with button controls on the endoscope handpiece, provides depth scanning from 0 to 250 um beyond the window surface. Images can be acquired at 0.7 s per frame at 1024 x 512 pixels or 1.2 s per frame at 1024 x 1024 pixels. The maximum output of the endomicroscope is 1 mW at 488 nm wavelength. The confocal microscopy component of the integrated endoscope system is 5 mm of the total 12.8 mm diameter. In addition to the confocal component, the integrated video-endoscope includes two light guides, an imaging CCD, a biopsy channel, air and water jet channels, and an additional water jet channel that is used for topical application of contrast agents, such as acriflavine. Table 4 summarizes the technical specifications of the Optiscan/Pentax ISC- 1000 confocal endomicroscope. The Pentax ISC-1000 system is designed for imaging the lower GI tract, but has also been used for imaging the stomach, duodenum, distal esophagus, and even the cervix [74-77].

The second clinically available endomicroscopy system is the Cellvizio (Mauna Kea Technologies, Paris, France), a probe-based endomicroscopy system. Confocal imaging is achieved through the use of miniprobes, that can be inserted in the accessory channel of any standard endoscope [78]. Unlike the distal scanning of the Pentax system, the Cellvizio incorporates a proximally scanned fiber bundle to deliver 488 nm wavelength laser light to the sample. An example fiber bundle employed by Mauna Kea

Technologies is composed of 30,000 optical fibers, with a fiber inter-core distance of 3.3 um and a fiber core diameter of 1.9 um [79].

The Cellvizio system is composed of a Laser Scanning Unit, a range of fibered objectives, and dedicated software which allows for obtaining images at a rate of 12 frames per second. The Cellvizio was developed using a 488 nm Sapphire laser, followed by another model which featured a 660 nm source for reflectance imaging [80]. Real time imaging is achieved using a 4 kHz oscillating mirror for horizontal line scanning and a galvanometric mirror for frame scanning, resulting in a raster pattern that is scanned across the surface of the fiber bundle [81]. A custom image processing algorithm is then used to correct for any artifacts that have occurred while imaging through a fiber bundle [81].

Imaging parameters of the Cellvizio system range with the variety of Confocal Miniprobes that have been developed for use with the base unit. These probes differ by their distal optics and their bundle characteristics and vary in flexibility, size, sensitivity, and resolution in order to meet the different clinical or research needs. Table 4 outlines the main characteristics of the different probes developed for clinical research [70]. Each probe also houses a small electronic chip which is used by the base unit for probe identification. The Cellvizio system does not allow for modification of the depth of the focal plane; the focal plane of each Confocal Miniprobe is fixed. However, the appropriate Confocal Miniprobe with a specific working distance can be selected for the application.

To make a general comparison between the two commercial systems, the Pentax ISC-1000 is a distally scanned confocal endomicroscope that is incorporated in a conventional video-endoscope, while the Cellvizio Confocal Miniprobes are proximally scanned probes that may be used independently or incorporated into any standard endoscope.

The Pentax reports excellent lateral and axial resolution for a fixed FOV. The miniO Cellvizio Miniprobe also has excellent lateral and axial resolution with a smaller FOV. If a greater FOV is necessary, resolution can be sacrificed by switching to a different Miniprobe. The Pentax has an axial scanning mechanism allowing the user toadjust the depth of theimage plane in the sample, whereas, the Miniprobes have fixed working distances.

The Cellvizio has a significantly faster acquisition rate than the Pentax, which can be critical for imaging in vivo. Additionally, Cellvizio has an outstanding software and image processing package, including video mosaicing to extend the image FOV.

CHAPTER III

PRECLINICAL MULTISCALE MULTIMODAL SYSTEM AND IMAGING*

Optical techniques can noninvasively probe biochemical and/or morphological changes associated with precancer progression, and are particularly amenable to epithelial tissues accessible by rigid or flexible endoscopes [82]. Additionally, optical techniques are applicable on a wide range of scales, from subcellular to organ level imaging. However, imaging systems are typically designed to either have a macroscopic view, sacrificing spatial resolution, or to have high resolution within a limited FOV. The ideal optical diagnostic would have high sensitivity macroscopic surveillance guiding high resolution and high specificity imaging for diagnosis.

High resolution imaging, such as confocal or nonlinear microscopy, provides information about tissue architecture and cellular morphology similar to histology [83, 84]. RCM uses spatial filtering through a confocal pinhole to remove out of focus scattered light, generating high resolution "optical sections" of tissue .The greatest source of RCM image contrast in the epithelium is variation in tissue refractive index, for example in the cell nuclei compared to the surrounding cytoplasm [85]. This enables visualization of cell nuclei and quantification of features such as the nuclear-to-cytoplasmic ratio, a morphological feature for diagnosis of oral epithelial dysplasia and

---

* Reprinted with permission from "FLIM and reflectance confocal microscopy for multiscale imaging of oral precancer" by Jabbour J. M., Cheng S., Malik B.H., Cuenca R., Jo J.A., Wright J., Cheng Y-S.L., Maitland K. C., 2013. Journal of Biomedical Optics, 18(4), p. 046012, Copyright [2013] by Society of Photo-Optical Instrumentation Engineers.

oral squamous cell carcinoma. Other morphological/ cytological features include large and prominent nucleoli, increased mitotic activity, abnormal mitoses, and cellular and nuclear pleomorphism. RCM has been demonstrated to distinguish these morphological changes between normal, precancerous, and cancerous oral tissue [86, 87]; however, RCM typically has a limited FOV and requires guidance on the macroscale. Guidance may be provided by visual inspection, which is highly dependent on the clinical experience of the examiner. Even for experienced clinicians, some early oral malignant lesions may be indistinguishable from benign lesions and premalignant lesions can be quite large and heterogeneous, complicating identification of the most severe site of disease for measurement. The combination of large FOV imaging for macroscopic surveillance with high resolution imaging or point measurement techniques has the potential to improve diagnosis and diagnostic yield by guiding the effective point sampling technique to the site with the most advanced state of disease within a lesion or the OC [88-91].

Wide-field autofluorescence imaging instruments are commercially available for clinical oral cancer detection [92, 93]; however, while they may be sensitive to biochemical changes in the tissue, differentiation of (pre)malignant from benign lesions remains a challenge [94, 95]. Because the overall fluorescence signal is dominated by stromal fluorescence which decreases with both inflammation and dysplasia, fluorescence from NADH and collagen need to be separated in order to differentiate between benign and precancerous lesions. The overlapping spectral properties of NADH and collagen complicate analysis based solely on fluorescence intensity.

Optical sectioning techniques, such as multiphoton microscopy, can spatially separate epithelial from stromal signal; however, slow acquisition time for three-dimensional scanning and small FOV result in similar disadvantages to RCM for screening of large organs, and with a higher system complexity and cost. The addition of lifetime measurements in large-FOV FLIM is another option to decouple contributions from different fluorophores, potentially providing a more accurate analysis of the metabolic activity in precancerous tissue over fluorescence intensity alone [96-98]. Moreover, the fluorescence lifetime is sensitive to the local microenvironment, serving as an additional indicator towards characterizing malignant transformation, and is less sensitive to intensity artifacts such as photo-bleaching and excitation power. The multispectral FLIM system presented here has the ability to simultaneously collect fluorescence intensity and lifetime images in three different channels corresponding to the peak emission wavelengths of NADH, FAD, and collagen, providing multiple biochemical indicators to characterize the specimen. A dual modality imaging system to detect both biochemical and morphological changes that are associated with oral precancer progression is presented here. Specifically, the integrated system uses FLIM to provide real-time wide-field, low spatial resolution images of the biochemical makeup of the specimen. These images then serve as a guide to direct RCM imaging to suspicious sites within the tissue. Coregistered RCM facilitates morphological imaging of the subcellular structure of the epithelium with small FOV but very high spatial resolution in three dimensions.

III.1. Multimodal multiscale imaging system

The multimodal optical system was designed to probe the biochemical properties of tissue on a macroscopic scale and the cellular morphology with high resolution. Therefore, largefield FLIM and high-resolution RCM subsystems are placed adjacently with a common sample translation stage for coregistration of images. A detailed schematic of our integrated system is shown in Fig. 6.

The wide-field FLIM subsystem was built following a previously reported multispectral time-domain scanning implementation [99]. It used an UV frequency-tripled Qswitched ND:YAG laser (355 nm, 1 ns pulse-width, 100 kHz maximum repetition rate, AOT-YVO-100QSP/MOPA, Advanced Optical Technology, Essex, United Kingdom) for excitation.

The laser light was coupled into a multimode fiber with a 50 μm diameter high – OH silica core (FVP050055065, Polymicro Technologies, Phoenix, Arizona). The fiber output was collimated and then reflected by DM1 (NC176741-z355rdc, T > 95% for 380 to 800 nm, Chroma Technology Corporation, Bellows Falls, Vermont) to a pair of close-coupled galvanometer mirrors (6200HM40, Cambridge Technology, Lexington, Massachusetts) for two-dimensional raster scanning. A UV-to-NIR corrected triplet (NT64-837, Edmunds Optics, Barrington, New Jersey) with a focal length of 45 mm and effective NA of 0.06 was used to focus light onto the sample.

The fluorescence emission was collected by the same triplet before being separated from the excitation light by DM1 and coupled into a multimode fiber with a

200 μm core diameter (BFL22-200, Thorlabs, Newton, New Jersey). The fiber output was collimated and separated into three spectral bands using two DMs (DM2, LM01-427-25, T > 95% for 439 to 647 nm, and DM3, FF484-Fdi01,T > 95% for 492 to 950 nm, Semrock, Rochester, New York).

The emission collection spectral bands were further specified by two bandpass filters (FF01-390/40, FF01-452/45, Semrock) and a long pass filter (FF01-496, Semrock) selected based on emission spectra of the three endogenous fluorophores of interest: collagen (F1: 390 +/- 20 nm), NADH (F2: 452 +/- 22.5 nm) and FAD (F3: >500 nm). The three emission bands were then temporally separated using three multimode fibers with lengths of 1, 13, and 25 m (BFL22-200, Thorlabs) providing a time delay of 60 ns between two consecutive spectral bands to allow measurement of the fluorescence lifetime in the three spectral bands with a single detector.

The outputs of the three fibers are then detected by a high-speed (180 ps rise time, 90 ps TTS) MCP-PMT (R5916U-50, Hamamatsu, Bridgewater, New Jersey), amplified by a preamplifier (C5594- 12, Hamamatsu) and sampled by a digitizer at 6.25 GHz (PXIe- 5185, National Instruments, Austin, Texas) using custom software programmed in LabVIEW (National Instruments).

The MCP-PMT signal collected at each pixel was 200 ns in duration and contained three consecutive fluorescence decays from the three spectral channels. The measured instrument response function was deconvolved from the measured fluorescence decays using the Laguerre deconvolution method.

For high resolution RCM, a NIR continuous wave diode-pumped solid state laser (1064 nm, 1 W, CL1064- 1W0, Crystalaser, Reno, Nevada) was used as the illumination source. A combination of a half-wave plate and a linear polarizer in the beam path served as a variable attenuator to control the optical power incident on the sample. A spatial filter in the beam path was used to produce a clean Gaussian beam.

An 8 kHz resonant scanner and a galvanometer scanner operating at 7 Hz (CRS 8K and 6215HM40, Cambridge Technology) were close-coupled to raster scan the NIR beam.

A 2× beam expander filled the back aperture of a water immersion 60×, 1.0 NA, 2 mm working distance microscope OL (LUMPLFLN60X/W, Olympus, Center Valley, Pennsylvania), which focused the light onto the sample. A combination of linear polarizer, polarizing BS, and quarter waveplate were used to remove specular reflections within the optical system.

Finally, a spatial filter with confocal pinhole of 30 μm diameter for optimized system characterization and 50 μm diameter for tissue imaging rejected out of focus light prior to signal detection by an APD module (APD110C, Thorlabs).

The generated voltage signal was digitized at 39.55 MHz by the digitizer, shared with the FLIM module. Position signals from the scanning mirrors were used as triggers for the confocal data acquisition and image formation. The images were corrected for the nonlinear sinusoidal scan of the resonant scanner and displayed in real-time.

To improve contrast for print viewing, RCM images were cropped and contrast-enhanced using ImageJ software (http://imagej.nih .gov/ij/, National Institutes of Health, Bethesda, Maryland).

An automated translation stage was used to move the sample between the FOVs of the FLIM and the RCM subsystems which are approximately 90 mm apart. A paper 1951 USAF resolution target (NT53-715, Edmund Optics) with a black pattern printed on a white background and a reflective positive USAF high-resolution target immersed in water (NT58-198, Edmund Optics) were used to measure FOV and lateral resolution of the FLIM and RCM modules, respectively.

Confocal axial resolution was measured by translating a planar mirror immersed in water through the focus in 0.5 μm steps and measuring the FWHM of the axial point spread function. The relative distance between the centers of the FOV's was also calibrated using a 1951 positive USAF resolution target placed on a white paper and was later used to acquire coregistered images from the two subsystems with lateral accuracy less than the FLIM lateral resolution.

The maximum background level in the FLIM system was evaluated by imaging a mirror placed in the FLIM focal plane.

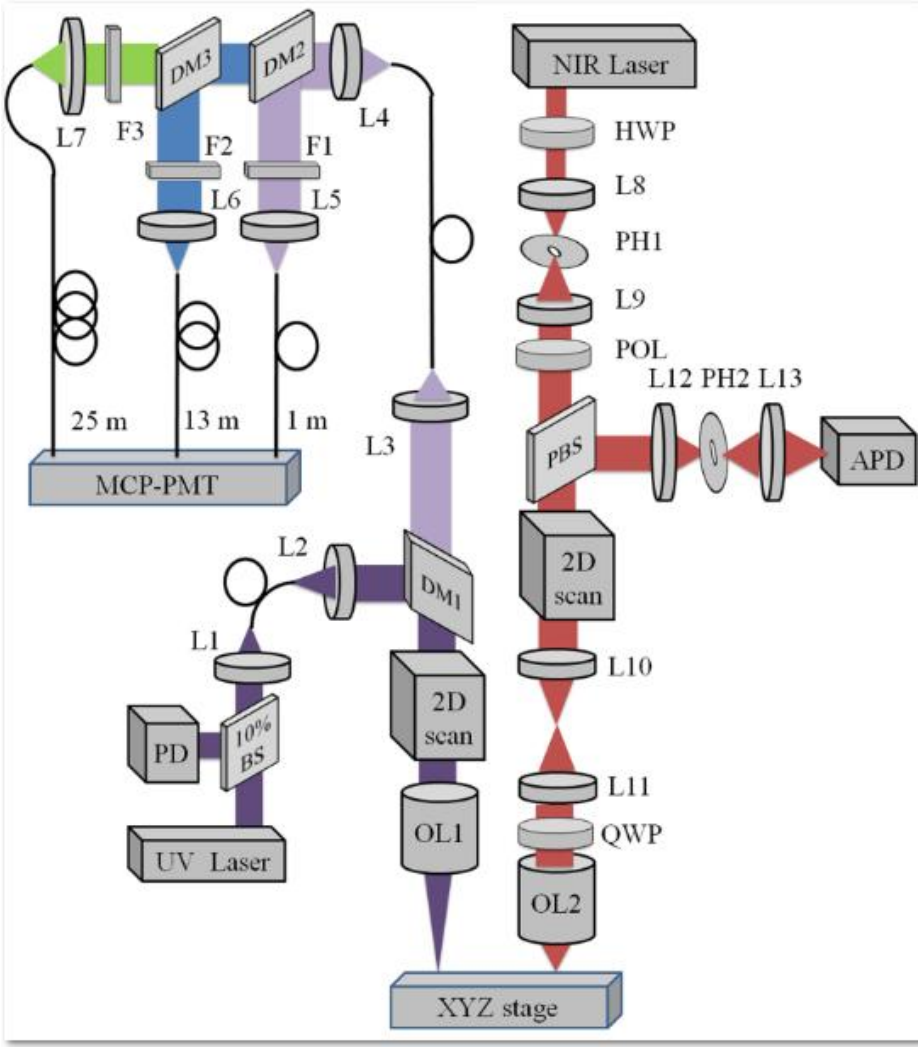

Figure 6: **Schematic of the combined FLIM-RCM system. Left: The FLIM module uses a UV pulsed laser, two galvanometer scanning mirrors, and a 45 mm focal length triplet lens (OL1). Three emission bands centered at 390 nm for collagen, 452 nm for NADH, and >500 nm for FAD are spectrally separated by DM and filters (F), temporally separated by three multimode fibers of 1, 13, and 25 m length, and detected by a single gated MCP-PMT. A 10 % BS and photodiode (PD) provide the trigger for data acquisition. Right: The RCM module uses a NIR laser, resonant and galvanometer scanning mirrors, and 1.0 NA OL (OL2). Spatial filters [lenses (L) and pinholes (PH)] are used in confocal illumination and detection, and signal is detected by an APD. A HWP and polarizer (POL) are used to control power, and a QWP and polarizing BS to reduce specular reflection. An XYZ translation stage co-registers FLIM and RCM images.**

The RCM-FLIM system was first characterized by imaging fluorescent and reflective USAF resolution targets. The FOV of the FLIM subsystem was set to be 16 × 16 mm2 while being able to distinguish element 1 of group 3 corresponding to a lateral resolution of 62.5 μm, as seen in Fig. 7(a), using 400 × 400 pixels per image and 10 KHz laser repetition rate. A single image acquisition time in the FLIM module takes 19.2 s. The temporal resolution of the FLIM system is calculated to be 320 ps based on the Nyquist theorem. The RCM system was measured to have a 400 μm diameter FOV [Fig. 7(b)] and a lateral resolution of 0.97 μm or less, based on resolution of element 1 of group 9 [Fig. 7(c)]. The FWHM axial resolution was measured to be 3.5 and 4.5 μm using 30 and 50 μm diameter pinholes, respectively. The larger pinhole was used for imaging tissue samples to increase signal to noise ratio.

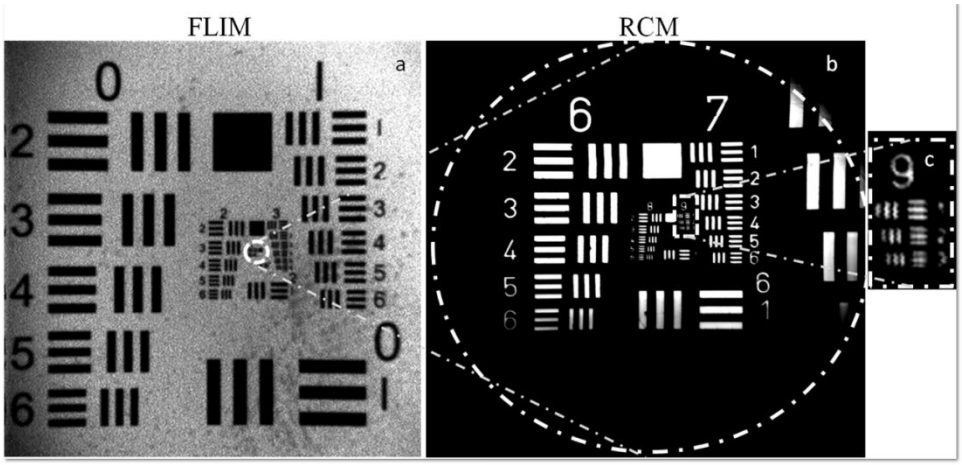

Figure 7: (a) 16 mm × 16 mm FLIM image of fluorescent positive USAF target. Element 1 of group 3, corresponding to a line width of 62.5 μm, can be resolved. (b) 400 μm diameter (dashed circle) RCM image of positive USAF target. Outlined region in (a) provides relative scale of the FLIM and RCM modalities. (c) Zoom in of group 9 in (b). Element 1, corresponding to a line width of 0.97 μm, is resolvable.

III.2 Oral mucosa imaging

III.2.a. Materials and methods

Porcine buccal mucosa is used as a model of human oral mucosa due to their similar epithelial thickness, nuclear size, and cell density. Healthy porcine tissue was obtained from a local slaughterhouse or through the tissue sharing program at TAMU, and transported to the lab for imaging within a couple of hours postmortem. 2 × 2.5 cm2 buccal mucosa tissue samples were excised from the inner cheek and placed in PBS solution prior to imaging. The pig tissue was at room temperature (~70°F) during imaging. After imaging, tissue samples from the imaged locations were obtained, fixed in 10% formalin, and processed for H&E histological comparison.

The hamster cheek pouch model of oral cancer was employed to evaluate in vivo imaging of premalignant oral mucosal tissue. Specifically, the hamster was imaged during the early stages of DMBA- induced oral carcinogenesis. A Golden Syrian hamster was used in this study. The animal use protocol was reviewed and approved by the TAMU IACUC, and a veterinarian oversaw the clinical aspects of this study. The hamster was housed in pathogen-free conditions and fed with rodent chow and water ad libitum. The right buccal pouch of the hamster was treated 3 times a week for 8 weeks with 0.5% solution of DMBA (Sigma-Aldrich) dissolved in mineral oil (Sigma-Aldrich). The left pouch was treated with mineral oil only and served as a normal control. At the time of imaging, the hamster was anesthetized using an intraperitoneal injection of 10% urethane solution. Once anesthetized, the hamster cheek pouch was pulled and clamped

into a custom built mount to expose maximum tissue area. During the imaging procedure, the anesthetized hamster was kept warm with a heating pad. The exposed cheek pouch was likely between room temperature and body temperature of the hamster. After imaging of the buccal mucosa, the hamster was euthanized with a solution of pentobarbital. The cheek pouches were then excised, fixed in 10% formalin, and processed for H&E histology.

Samples were first imaged with the FLIM module, then positioned for confocal imaging. Pig and hamster tissue were treated with vinegar (5% acetic acid) for 1 to 2 min following FLIM imaging and prior to RCM imaging. Application of acetic acid results in an increase in scattering by the nuclei, termed acetowhitening, and thereby improves the contrast and the ability to delineate nuclei within the surrounding cytoplasm in RCM imaging [100, 101]. Apple cider vinegar has the same acetowhitening effect and has previously been used as a better tasting alternative to white vinegar for in vivo confocal imaging of the oral mucosa in humans [86]. The samples were translated in 2 to 3 μm axial steps to acquire 3D confocal data. RCM data were acquired at six sites within the pig cheek distributed across the FLIM imaging area. In the DMBA-treated hamster cheek pouch, spatial features in the FLIM intensity and lifetime images were used to guide RCM data acquisition. Fifteen sites were imaged with RCM in the treated pouch, and three sites were imaged in the contralateral normal pouch.

For all samples, the pulse energy of the 355 nm laser was set to be ~1 μJ/pulse which corresponds to an average power of 10 mW at the sample. The maximum illumination power at the sample from the 1064 nm laser was set below 45 mW. These

values are below the maximum permissible exposure for skin at the corresponding wavelengths.

One major challenge of validation studies of optical imaging techniques, particularly small FOV imaging, is accurate correlation with histology. The FLIM-RCM system software recorded the mapping coordinates of RCM imaging sites for accurate registration to the FLIM image and for localization relative to the edge of the tissue mount. However, it was very difficult to completely immobilize the approximately 16 × 16 mm2 specimens when sectioning them for histologic processing. This could potentially result in some inherent error in coregistration of the imaging sites and the corresponding histology sections, especially for the confocal imaging sites due to the relatively small FOV.

III.2.B. Results

The RCM images in Fig. 8(g) to 8(i) clearly show the epithelial cell nuclei as bright spots on a darker background. The media file shows RCM video as the image plane is translated from the tissue surface to 300 μm in depth (Video 1). Both the nuclear density and nuclear-to-cytoplasmic ratio increased with depth in the epithelium, which is a hallmark of normal epithelium. Cell nuclei were detectable in RCM images down to a depth of 300 μm below the surface. Figure 8(j) shows an H&E histology image of a tissue sample taken from the region imaged. The size and spatial distribution of nuclei in the en face confocal images correlates well with the cross-sectional histology image.

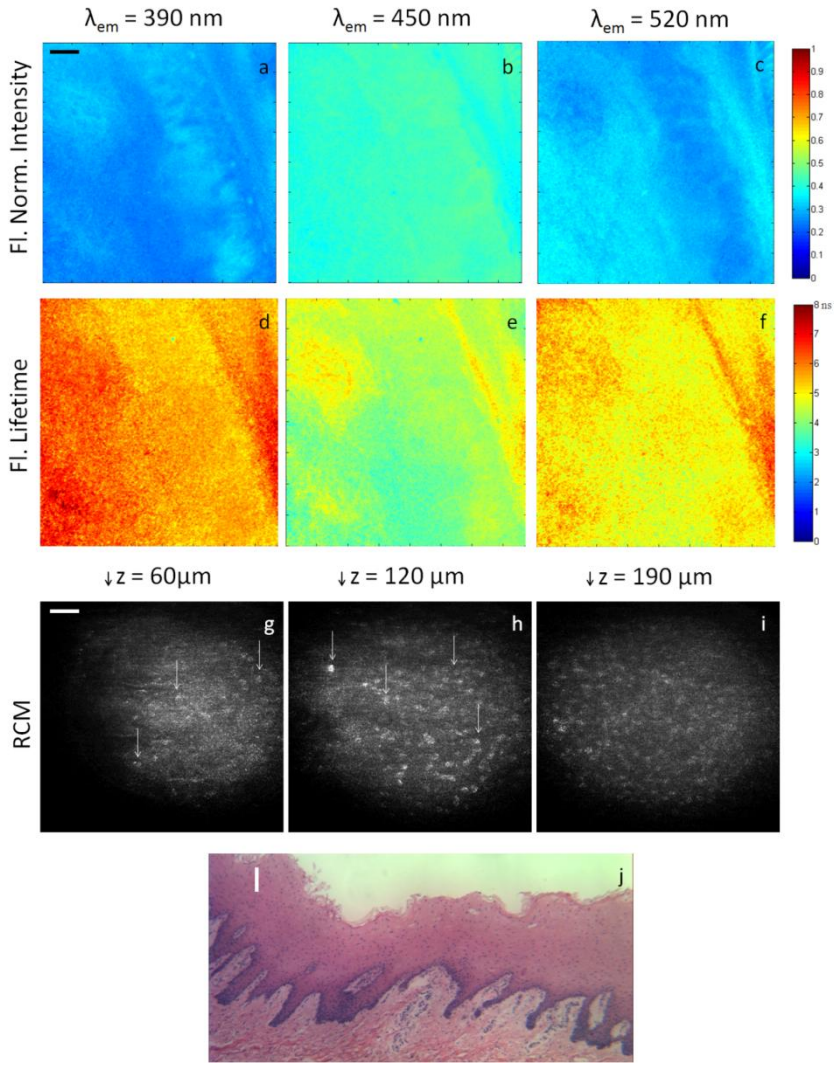

Figure 8: ***Ex vivo*** **FLIM-RCM images of normal porcine buccal mucosa. FLIM normalized intensity maps at (a) 390 nm, (b) 452 nm, and (c) >500 nm. FLIM average lifetime maps at (d) 390 nm, (e) 452 nm, and (f) >500 nm. Arrows identify the RCM imaging location at the center of the FLIM FOV. RCM images obtained at (g) 60 µm, (h) 120 µm, and (i) 190 µm depths. The corresponding video shows RCM images scanning from the surface down in depth to 300 µm (Video 1). Arrows point to individual nuclei. (j) 10× H&E histology image of tissue. Scale bars: (a) 2 mm, (g) 50 µm, and (k) 100 µm. (Video 1, QuickTime, 3.3 MB).**

Figure 9 shows multispectral FLIM, RCM, H&E histology, and photograph images of normal [Fig. 9(a) to 9(k)] and precancerous hamster cheek pouch treated with DMBA carcinogen [Fig. 9(l) to 9(z)]. Histopathological diagnoses of sections spanning

the entire imaging area in the treated pouch include normal, cytologic atypia, low-grade dysplasia, high-grade dysplasia, and cancer [papillary tumor in the lower right quadrant of Fig. 9(r)]. Figure 9(a) to 9(f) shows the normalized fluorescence intensity and average lifetime maps for the normal hamster cheek pouch.

The RCM images taken from the center of the FLIM FOV at approximate depths of 18 μm [Fig. 9(h)] and 39 μm [Fig. 9(i)] show scattering from the keratin at the surface and epithelial nuclei beneath this superficial layer. Figure 9(j) is a zoomed in view of Fig. 9(i) to more clearly show the cell membranes and nuclei identified by arrows. Figure 9(l) to 9(q) shows the normalized fluorescence intensity and average lifetime maps for the DMBA-treated hamster cheek pouch. As seen in the corresponding photograph of the tissue in Fig. 9(r) and in the FLIM images, a tumor is visible in the lower right quadrant of the tissue.

RCM imaging was performed in a number of locations throughout the cheek pouch, two of which are identified by arrows labeled "1" and "2" in the FLIM images. Region 1 was later diagnosed as cytologic atypia [Fig. 9(v)] and region 2 was diagnosed as low-grade dysplasia [Fig. 9(z)] by histopathology. The RCM images of region 1 just below the surface [Fig. 9(s)] and deeper in the epithelium [Fig. 9(t) and Fig. 9(u) zoomed in] show very small features that may be epithelial nuclei or possibly nucleoli that can be seen in the corresponding histology section in Fig. 9(v). In contrast, the RCM images of the epithelium in region 2, shown in Fig. 9(w) and 9(x) and Fig. 9(y) zoomed in, show much larger nuclei indicative of precancerous changes. Arrows in RCM images identify cell nuclei. These results illustrate that RCM allows identification of cellular

changes from two pathologically different regions in areas that look abnormal but similar based on FLIM imaging.

The results from the high-resolution RCM demonstrate the potential of the imaging system towards characterization of subcellular morphological features of the epithelial tissue. The brighter nuclei against the darker background can be delineated in the RCM images and videos. The normal cell nuclei in the porcine tissue are on the same scale as normal human epithelial cell nuclei. Although normal hamster epithelial nuclei are smaller, they are still detectable with our RCM imaging system. An increase in nuclear size was distinguished between normal and dysplastic tissue in hamster cheek pouch. RCM images of epithelial nuclei can be further analyzed either manually or through automated image processing to calculate more objective parameters defining epithelial tissue characteristics such as nuclear size, nuclear density, and nuclear-to-cytoplasmic ratio.

The RCM system was able to distinguish between two pathologically different regions that look the same (abnormal) using FLIM. This shows the importance of these two complementary techniques.

Figure 9: ***In vivo*** **FLIM-RCM images of (a-k) normal and (l-z) DMBA-treated hamster cheek pouch. Normalized FLIM intensity maps at (a, l) 390 nm, (b, m) 452 nm, and (c, n) >500 nm spectral bands. FLIM average lifetime maps at (d, o) 390 nm, (e, p) 452 nm, and (f, q) >500 nm spectral bands. (g, r) Photographs of FLIM imaging areas. Arrows in FLIM and photo images correspond to regions for subsequent RCM images. Arrows labeled 1 and 2 in (l-r) correspond to Regions 1 (s-v; cytologic atypia) and 2 (w-z; low-grade dysplasia), respectively. RCM images (h, i, s, t, w, and x) taken at indicated depths. Zoom in RCM images (j, u, and y) taken from dotted squares in (i, t, and x), respectively. Arrows in RCM images indicate nuclear features. Corresponding video shows RCM images scanning in depth in region 2 (Video 2). (k, v, and z) 25× H&E histology images from RCM regions. Scale bars: (a, g) 2 mm, and (h, j, and k) 50 µm. (Video 2, QuickTime, 1.0 MB).**

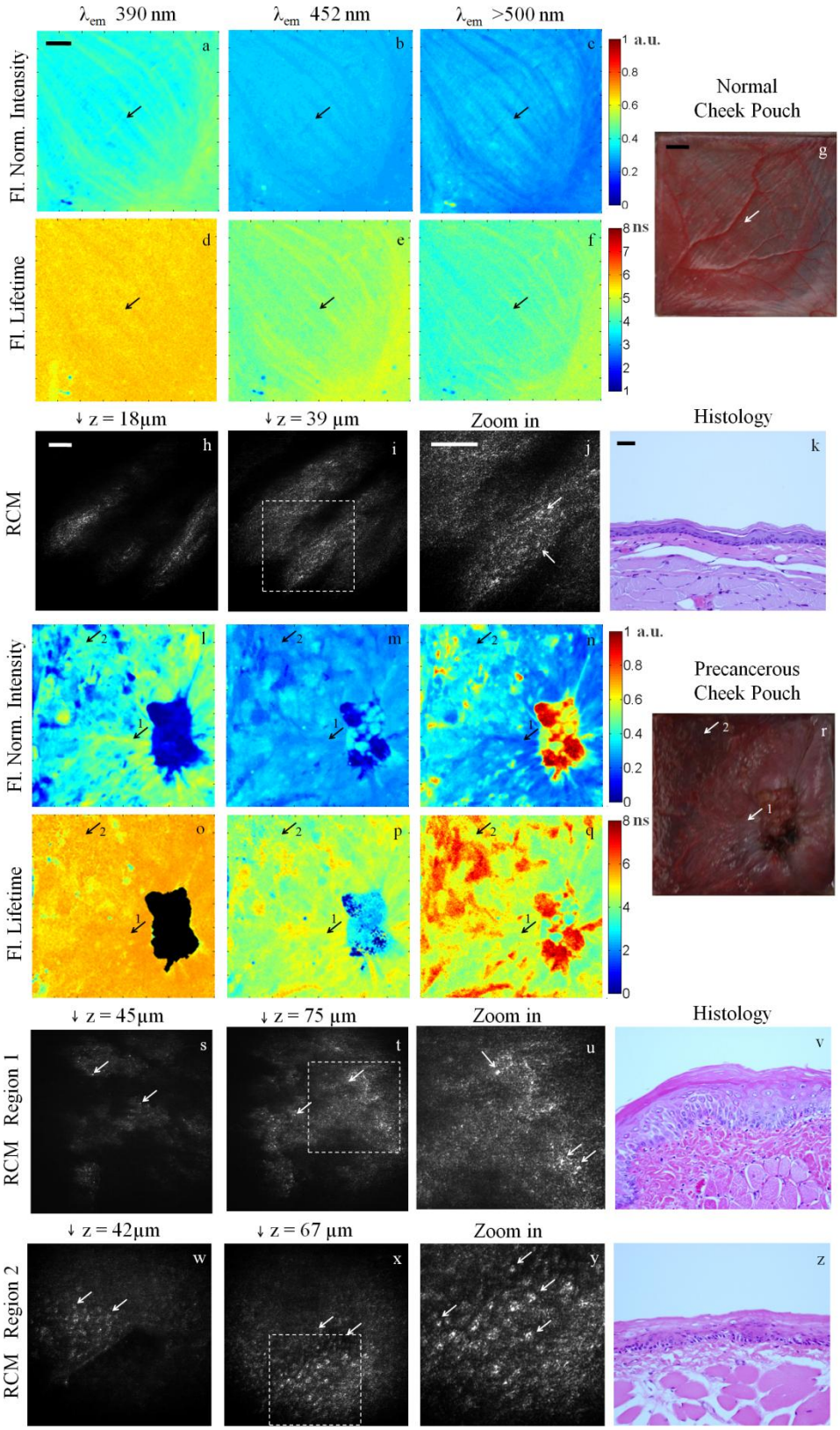
λem 390 nm
λem 452 nm
λem >500 nm
Fl. Norm. Intensity
Fl. Lifetime
a.u.
ns
Normal
Cheek Pouch
↓ z = 18µm
↓ z = 39 µm
Zoom in
Histology
RCM
Precancerous
Cheek Pouch
↓ z = 45µm
↓ z = 75 µm
RCM Region 1
↓ z = 42µm
↓ z = 67 µm
RCM Region 2

CHAPTER IV

AXIAL SCANNING IN CONFOCAL MICROSCOPY USING AN ETL*

After testing the system in preclinical studies, it was time to transition to the clinical studies therefore a more compact clinical confocal microscope was needed for the use in the clinic. The new RCM scope that was built consisted of a new compact version of the big benchtop system with a new miniature lens used with ETL scanning for in vivo imaging.

Various axial scanning mechanisms have been implemented for benchtop and endoscopic laser scanning imaging systems to obtain volumetric images of biological tissue. These techniques can be divided into two categories. The first category requires moving the sample or the OL relative to the other using translational stages or hydraulic, pneumatic or mechanical scanners [102-104]. The other category does not require any mechanical movement and utilizes moving and shaping of focus and/or wavefront by exploiting chromatic aberrations [105, 106], using adaptive phase compensation techniques [26, 54, 107], or utilizing a variable focal length lens [108]. These "optical axial scanning" mechanisms can enable relatively faster axial scanning that is less susceptible to motion artifacts in smaller package endoscopes.

---

* Reprinted with permission from "Optical axial scanning in confocal microscopy using an electrically tunable lens" by Jabbour J.M., Malik B.H., Olsovsky C., Cuenca R., Cheng S., Jo J.A., Cheng Y.S.L., Wright J.M., and Maitland K.C., 2014. *Biomedical Optics Express,* 5(2), 645-652, 2014, Copyright [2014] by OSA.

Although focus tunable lenses have been implemented in nonlinear microscopes [108], the use of these lenses for axial scanning in confocal microscopy is more complicated because of the collection pinhole, and therefore, both the illumination and the detection pathways are affected. Beyond nonlinear microscopy, focus tunable lenses have recently been used for three-dimensional optical tweezers, three-dimensional light-sheet microscopy with increased scanning speed [109], focus control in wide-field endoscopy [110], and zoom lens design with no moving parts [111].

To achieve axial scanning in a RCM, a commercially available ETL, wherein the focal length can be varied as a function of the supplied electrical signal, is used. The optical properties of RCM incorporating an ETL were characterized and lateral and axial resolutions were quantified over the axial scan range of such a system. The performance was further demonstrated by imaging of fresh tissue biopsies from the human OC *ex vivo* and normal skin tissue *in vivo*.

The confocal microscope used in this paper is a modified version of the system described in detail previously [2]. An 811 nm continuous wave laser (DL808-120-0, Crystalaser, Reno, NV) is used for illumination. A linear polarizer and a HWP are used to control the laser power at the sample. The laser beam is raster scanned by two closely spaced scanning mirrors (CRS 8 KHz resonant scanner and 6215HM40 galvanometer scanner, Cambridge Technology, Bedford, MA). The two scanners are followed by a 2□ beam expander (AC127- 025-B-ML and AC127-050-B-ML, Thorlabs Inc., Newton, NJ) relaying the mid plane between the two mirrors onto the back focal plane of a microscope OL (CFI Apo 40XW NIR, Nikon). A QWP is placed before the OL which,

along with a polarizing BS in the detection path, reduces specular reflection from the optics. The detection arm consists of a lens (AC256-075-B-ML, Thorlabs Inc.) focusing light onto a 75 μm pinhole followed by another lens (AC256-030-B-ML, Thorlabs Inc.) relaying the in focus light onto a photomultiplier tube (H9305-03, Hamamatsu Corporation, Bridgewater, NJ). A digitizer is used for signal collection, digitization at 39.55 MHz and real-time corrected image formation at a frame rate of 7 Hz. To achieve axial scanning, an ETL should ideally be placed at the back focal plane of the OL. However, the ultimate application of this system is to image the human oral mucosa *in vivo*, and therefore, the imaging arm of the microscope is being designed to incorporate a rigid and relatively thin probe using a miniature OL to facilitate access in the OC. While the ETL employed in our system (EL-6-18, Optotune AG, Switzerland; 18 □ 19.3 □ 8.7 mm3) is one of the smallest tunable lenses commercially available, placing it adjacent to the OL would constrain the size of the probe. Therefore, in this study, the ETL was positioned as close as possible to the scanning mirror mount, near the image of the back focal plane of the OL, in order to provide a proof-of-concept for confocal endomicroscopes. Figure 10 depicts the Zemax (Radiant Zemax, Redmond, WA) model of the illumination arm incorporating the Zemax model of the ETL, downloaded from the Optotune website (http://www.optotune.com/). Because the OL prescription data was unavailable, a simplified 5 mm focal length lens (L1) was used as the OL in the design. Zemax designs for L1, L2, and L3 were downloaded from the Zemax lens catalog.

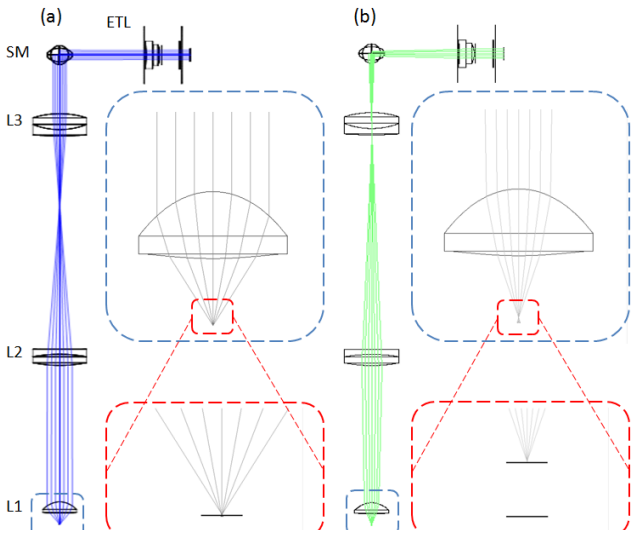

Figure 10: Zemax design showing the illumination arm of the confocal system including the ETL positioned adjacent to the scanning mirrors (SM). With negative ETL focal lengths, the imaging planes lie further from the lens or deeper in the sample (a), and with positive ETL focal lengths, the imaging planes lie closer to the lens and sample surface (b). The insets show the change in the NA and focal position at the sample space as ETL changes focal length from (a) *f* = -127 mm to (b) *f* = +44.3 mm. L1: Simplified OL, L2/L3: beam expander.

The focal length, *f*, of the ETL can be tuned from $f = -127$ mm, increasing in magnitude through collimation ($f = \infty$), and decreasing to $f = +44.3$ mm. The theoretical scan range in the sample space of the confocal microscope can be calculated using the combined effective focal length of the OL ($f = 5$ mm) and the ETL. Tuning the ETL from negative to positive focal lengths corresponds to an effective focal length scan range of 5.2 mm [Fig. 10(a)], through 5 mm (ETL $f = \infty$), to 4.5 mm [Fig. 10(b)]. Therefore, a full scan of the ETL corresponds to a theoretical axial scan range of ~700 μm in the sample space of the microscope. To measure the axial scan range and to compare the axial ETL-scanned imaging capability with that of traditional stage scanning, an automated translation stage was used to move the sample. While controlling the current to the ETL in 25 mA increments, the stage was positioned to

bring a planar reflective Ronchi ruling in focus, and the corresponding relative position of the stage was recorded. The resolution and image quality degrade significantly at high control current. This can be primarily attributed to inherent aberrations caused by the lens at very high control currents and very low positive focal lengths. Furthermore, the focus of the beam in the conjugate image plane between L2 and L3 scans within the lens L3 element at high current, as seen in Fig. 10(b). Therefore, the image quality was characterized over the practical current range of 0 to 150 mA to maintain acceptable image quality. This control current range corresponds to an axial scan range of 255 μm in sample space as shown in Fig. 11. The relative focal or axial position as a function of control current can be fitted to a polynomial equation $z = -0.0091i2 - 0.297i + 38$ (1) with R2 = 0.9991, where i is the current in mA and z is the axial distance in μm away from the nominal focal position of the OL.

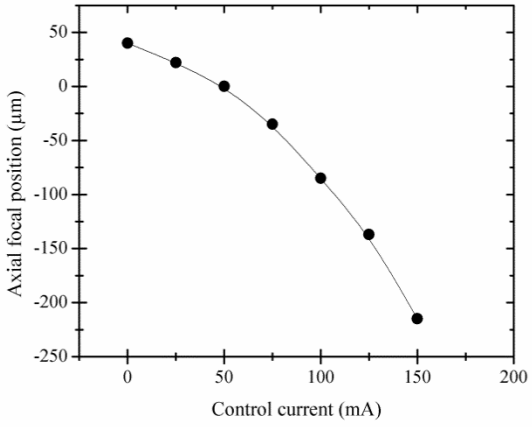

Figure 11: Measured axial position of the focal plane of the confocal microscope relative to the nominal focal position of the OL as a function of ETL control current. 50 mA of ETL current corresponds to no focusing power of the ETL ($f = \infty$) and the focus in sample space positioned at the working distance of the OL. Increasing axial position indicates increased depth in the sample. 150 mA ETL control current corresponds to an axial focal position above the nominal focal position by 215 μm. 0 mA ETL control current corresponds to an axial focal position below the nominal focal position by 40 μm.

The effect of the ETL scan on image magnification was characterized as a function of axial position of the object. Without the ETL or with the ETL focal length set to infinity, the total magnification of the microscope is 30 and the FOV is ~625 μm. The magnification varies from a factor of 1.03□ at $z = 40$ μm to 0.87□ at $z = -215$ μm, which is less than 20% change over the 255 μm scan range. The maximum change in system vignetting with ETL focal length change is measured to be 23%. To characterize the image quality throughout the axial scan, the lateral and axial resolutions were measured at different focal positions spanning the axial scan range. Imaging a reflective positive high-resolution US Air Force test target immersed in water, the smallest elements in group 9 element 3, corresponding to line widths of 775 nm, are clearly visible over the entire 255 μm axial scan range. Using the intensity profile crossing the edge of a group 6 element 6, the FWHM lateral resolution was measured using the derivative of the edge-response function, which corresponds to the cross section of the point spread function [112]. The FWHM axial resolution was measured by translating a planar mirror immersed in water using the translation stage in 0.5-μm axial steps for each of the ETL fixed focal positions. The results are summarized in Fig. 12, which shows both the theoretical and the experimentally measured lateral and axial resolution values along the 255 μm axial scan range. Without the ETL, the theoretical lateral and axial resolution of the microscope are 0.46 and 4.2 μm, respectively. As the focal depth decreases, shifting the focal position closer to the OL, lateral and, more significantly, axial resolution increase. This loss in image quality, also evident in the theoretical axial resolution plot in Fig. 12, can be attributed to reduced NA as the beam diameter entering

the OL decreases, as illustrated in Fig. 10. In addition to more spherical aberrations at higher control current, the ETL becomes more sensitive to misalignment yielding coma. Furthermore, the vertical orientation of the ETL within the system results in intensified aberrations due to effects of gravity on the liquid lens. The resultant change in resolution across different imaging depths is in agreement with the features seen during imaging of oral epithelium and discussed below.

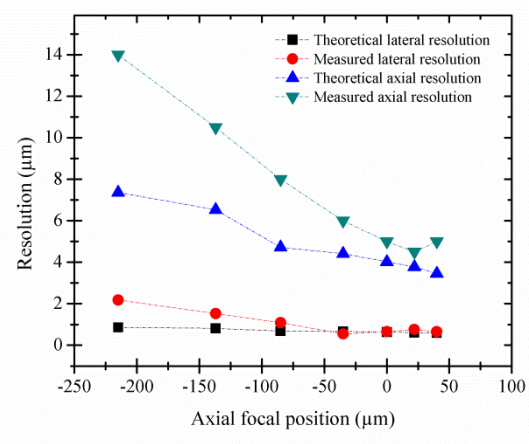

Figure 12: Theoretical and measured FWHM lateral and axial resolutions as a function of focal position.

To demonstrate the performance and application of the ETL in RCM, imaging was performed *ex vivo* on biopsy tissue from the human OC clinically diagnosed as inflammatory gingival hyperplasia using ETL scanning and traditional stage scanning for comparison. To further demonstrate ETL scanning speed *in vivo*, imaging of healthy skin was performed on the lateral nail fold of a finger. The imaging protocols were reviewed and approved by the IRB at TAMU and TAMU Baylor College of Dentistry. After tissue excision from the OC, the biopsy tissue was transported from the clinic to

the laboratory in PBS solution on ice and was imaged within one hour of excision. Before imaging, the biopsy tissue was soaked in vinegar for one minute which can increase the contrast between the nuclei and the cytoplasm of the epithelial cells in RCM imaging [100]. Following imaging, the biopsy tissue was fixed, processed for histopathology, and diagnosed as inflammatory fibrous hyperplasia. For RCM imaging of the oral biopsy, the tissue was mounted using small tweezers and immersed in sterile PBS solution in a petri dish placed on the translation stage. The biopsy tissue was first imaged with stage scanning in axial steps of 2 μm, while the ETL control current was set to 50 mA ($f = \infty$). Subsequently, the translation stage was positioned so that the image plane was approximately 150 μm below the surface of the tissue. The same location in the biopsy tissue was then imaged using ETL axial scanning with a scan frequency of 0.1 Hz and axial scan range of 177 μm within the tissue. To directly compare RCM images of tissue acquired using ETL scanning to those acquired with stage scanning, images from corresponding depths within tissue were selected and compared. To improve contrast and visualization of subcellular features, all images and corresponding media were cropped and contrast-enhanced using ImageJ software (http://imagej.nih.gov/ij/, National Institutes of Health, Bethesda, MD). Figure 13 (Video 4) shows images and videos obtained with both stage scanning [Figs. 13(a), 13(b), 13(e), 13(f), 13(i), and 13(j)] and ETL scanning [Figs. 13(c), 13(d), 13(g), 13(h), 13(k), and 13(l)] at increasing depth below the surface of the oral biopsy tissue. In the images and videos, the epithelial nuclei can be seen as bright spots. In the superficial cell layers, the cell borders can be seen as relatively bright lines around the darker cytoplasm

surrounding the nuclei. The dense chromatin in the cell nuclei, as characterized by hyperchromatism in the histology image, in addition to the aceto-whitening effect, favors the visualization of clear and bright nuclei in RCM images. As the axial scans approach greater depths in the tissue, it can be seen that the cytoplasm (darker area) shrinks and the nuclei become more closely spaced. This is characteristic of oral epithelial tissue wherein the cells show maturation from the deeper basal layers to the superficial layers of the epithelium, and therefore, the nuclear-to-cytoplasmic ratio and the nuclear density increase with depth in the epithelium. The top surface of the papillary region of the lamina propria between the rete ridges at the base of the epithelium can be seen as relatively darker areas in the deeper layers of the tissue (identified by arrows). Note that at any given time during the scan, the tissue does not completely fill the FOV. This is due to the specific location of the tissue being imaged not being completely flat relative to the image plane; the surface of the tissue in the top left of the FOV is above the surface in the center. The depths assigned to the confocal images shown in Fig. 13 were based on the tissue surface defined at the center of the image. In the corresponding histology image in Fig. 13(m) (cut vertically through the mucosa in comparison to the *en face* image orientation of RCM), the distribution of the darkly stained nuclei from the superficial layer to the base of the epithelium and the rete ridges distribution correspond well with RCM images. To demonstrate *in vivo* imaging using ETL scanning, the skin of the lateral nail fold was imaged on a normal volunteer's finger. The finger was positioned on the stage for support to minimize motion, and ultrasound gel (refractive index of 1.3526) was used as an indexmatching medium between the skin and the OL.

RCM video was acquired with ETL axial scanning at 0.2 Hz using a triangular control signal and an axial scan range of 177 µm.

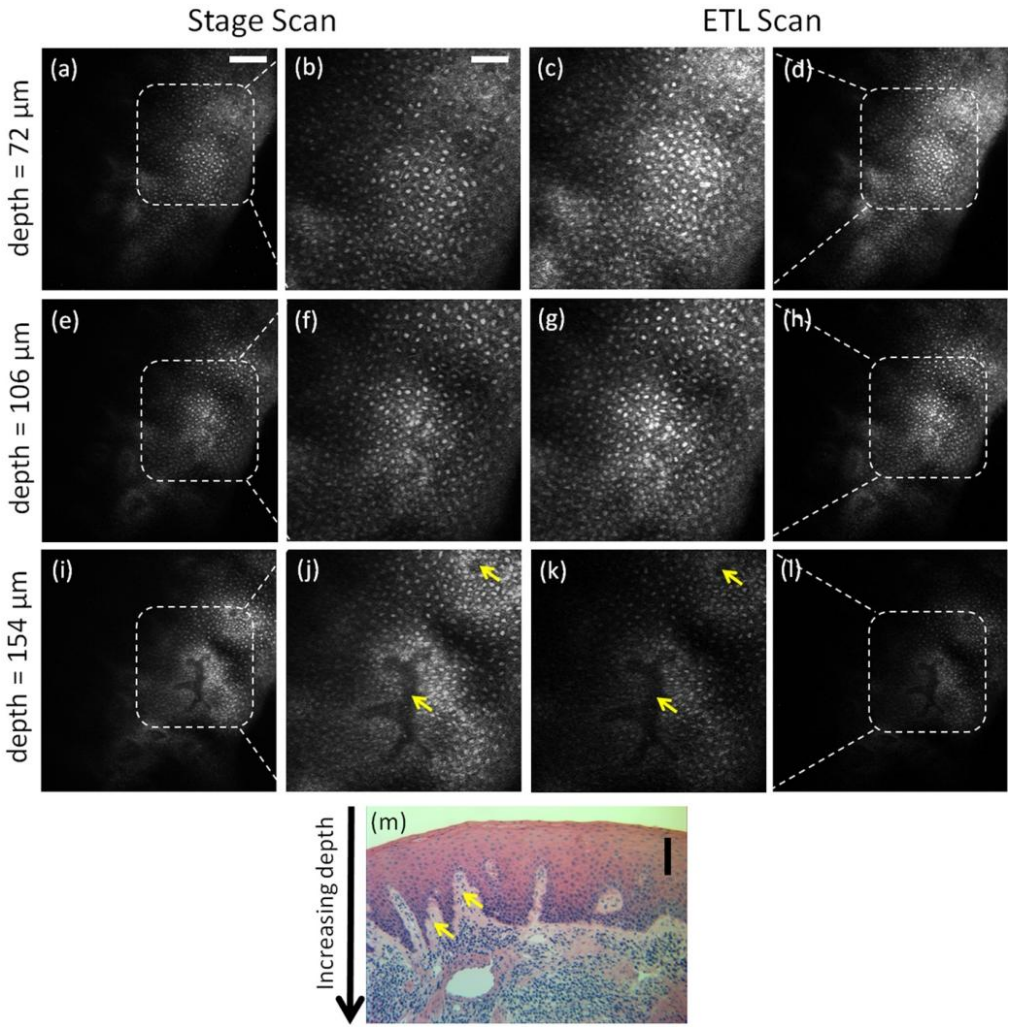

Figure 13: Confocal images and video (Video 4) from stage scan (a,b,e,f,i,j) and ETL scan (c,d,g,h,k,l) through oral mucosa taken from 72 µm (a-d), 106 µm (e-h), and 154 µm (i-l) below the surface of the tissue, corresponding to axial focal positions of z = 33, 11.5, and -35 µm, respectively. Zoom in images (b,c,f,g,j,k) clearly show nuclei as bright spots surrounded by dark cytoplasmic media. Corresponding histology image is shown (m) cut vertically through the epithelium. Arrows in confocal and histology images point to papillary regions of connective tissue between rete ridges. Scale bars: 100 µm in (a) for (d,e,h,i,l), 25 µm in (b) for (c,f,g,j,k), and 100 µm in (m).

The effect of degradation of resolution near the surface of the sample can be visualized in the superficial layer of the oral epithelium [Figs. 13(b) and 13(c)]. Cell

nuclei appear slightly more crowded in the ETL scanned image near the surface primarily due to worse axial resolution (~10 μm for ETL versus ~5 μm for stage scanning), and cell borders are slightly blurred likely due to worse axial and lateral resolution. This effect is less evident as the ETL scanned focal plane increases in depth and axial and lateral resolutions improve [Figs. 13(f), 13(g), 10(j), and 13(k)]. Degradation in resolution near the surface of tissue is preferable over worse resolution deeper in tissue because nuclei are typically less densely packed in the superficial layers and more crowded near the basement membrane. Furthermore, as the light passes through the epithelium, tissue scattering and wavefront distortion further degrade resolution at deeper depths. One advantage of ETL over other conventional axial scanning mechanisms is the ease of focal position control and speed at which focal position can be adjusted. Depending on the need of the application, the axial scanning can be set to scan slowly and continuously in depth, scan rapidly at speeds to avoid motion artifacts, or jump from discrete depth to depth to capture multiple frames at depths spaced further apart. The response time of the Optotune EL-6-18 lens is less than 2 ms with a settling time less than 10 ms allowing a scan rate of 100 Hz or more.

CHAPTER V

CLINICAL RCM WITH MINIATURE LENS AND ETL

The focus of this study was the design and evaluation of a miniature microscope objective lens which can provide high resolution RCM imaging of the epithelial tissue *in vivo*. The design specifications of the miniature lens, the manufacture and assembly methods, and the experiments and measurements to test the performance of the lens are described here. The overall design was geared towards imaging of the human oral cavity for detection of pre-cancer *in vivo*, which is the ultimate application of this RCM system. Nevertheless, the size and weight of the system renders our system light-weight and portable, and can easily allow imaging for other diseases of the epithelium such as that of skin, cervix and rectum. The lens is designed to be used in direct contact with the tissue which can potentially reduce motion artifact. The proof-of-concept demonstrates and enables the technique of RCM for potential disease detection and diagnosis *in vivo*.

The model and the specifications of the complete clinical confocal system are shown in figure 14 and table 6, respectively. The rigid reflectance confocal imaging system consists of a handheld box (110mmx110mmx70mm) followed by a rigid endoscope tube (~60mm length) with a tip of 6.4 mm outer diameter that will be in contact with the tissue. The source and detector are fiber coupled and placed on a separate bench. An 807 nm continuous wave laser (DL808-120-0, Crystalaser) beam is delivered by a polarization maintaining single mode fiber (P1-780PM-FC-2, Thorlabs) followed by a fiber lens collimator (TC12FC-780, Thorlabs) inside of the housing of the handheld imaging system. A laser power supply with adjustable output power from the

laser controls the laser power at the sample. The laser beam is raster scanned by two closely spaced scanning mirrors (CRS 8 KHz resonant scanner and 6200H galvanometer scanner, Cambridge Technology). The two scanners are followed by a 2x beam expander (AC127-025-B-ML and AC127-050-B-ML, Thorlabs) relaying the mid plane between the two mirrors onto the back focal plane of a custom miniature OL (Optics Technology). The design and performance of the miniature OL has been reported elsewhere. An ETL (EL-6-18, Optotune) is positioned as close as possible to the scanning mirror mount, near the image of the back focal plane of the OL. The detection arm consists of a fiber port collimator having XYZ tip tilt adjustments (PAF-X-11-PC-B, Thorlabs) focusing light onto a 10 µm core diameter multimode fiber (M64L02, Thorlabs) delivering in focus collected light to a photomultiplier tube (H9305-03, Hamamatsu Corporation). The photomultiplier tube is followed by an amplifier (C9999, Hamamatsu Corporation), which output is acquired by a NI digitizer computer for real time image generation.

Table 6: Clinical confocal system specifications

Lateral Resolution	1.4-1.9 microns
Axial Resolution	5-11 microns
Optical Axial Range	200 microns
Wavelength	807 nm
Frame Rate	7 Hz
FOV	550 microns
Imaging Mode	Reflectance

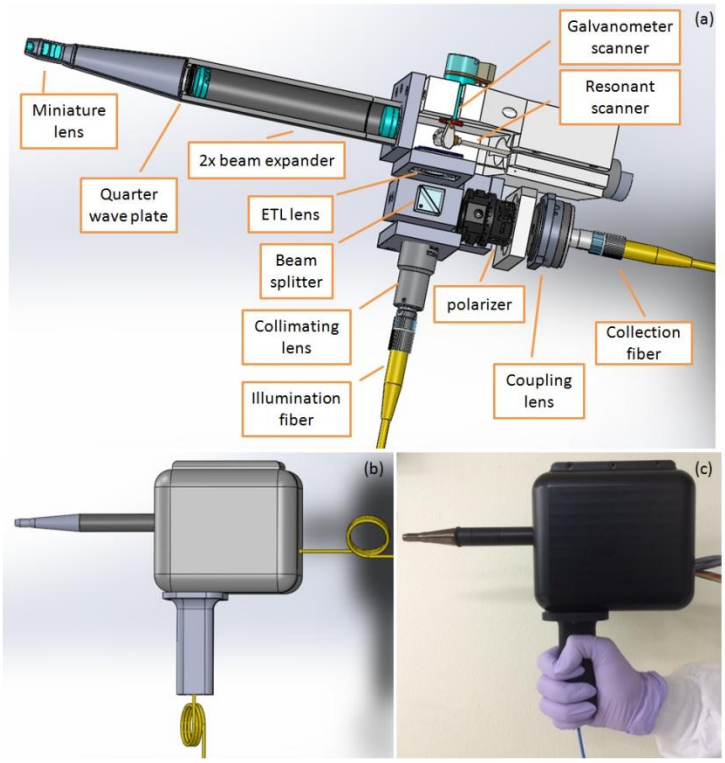

Figure 14: (a) Solidworks model of the housing and the inside of the confocal imaging system. (b) Model and (c) Photo of the plastic housing the RCM.

The outer case looks like a gun type handheld system to provide easier carry and grip by the doctor. The outer housing is made out of Delrin plastic for both robustness and lightweight. Custom mounts for the optics were designed, using SolidWorks 3D modeling software, to hold each optical component, with basis of alignment of optics, and be assembled together. All parts were manufactured out of Aluminum at the TAMU Biomedical Engineering machine shop.

The system is placed on a mobile cart to give easy access to different patient chairs at the clinic. The cart has on its top shelf a laser head and a photomultiplier for easy connection to the fibers connected to the handheld confocal system. XYZ stages are

placed on the top shelf to help position any biopsy that is to be imaged ex vivo after in vivo imaging. The cart has on lower shelves the digitizer computer, the power supplies and the electronics control box of the system.

The software interface allows the change of FOV by changing the scanning angles of the scanners. It also allows the change of focus planes inside the sample by changing the control current to the ETL: options of 0, 35, 95, 135 and 200 microns below the surface are available for the user to choose from. The axial scanning speed is set to 0.2 Hz to get 17 confocal images from different depths within 200 microns thickness of tissue. Changing of this axial scanning speed is possible by changing the frequency of the control current to the ETL.

The miniature microscope objective is designed to work jointly with an electrically focus tunable lens (ETL) in a reflectance confocal system for *in vivo* three-dimensional imaging in the oral cavity. Figure 15 shows a schematic of the integrated confocal system. The lens is designed to be used with a wavelength of 811 +/- 5 nm to exploit the enhanced penetration depth of near infrared light in tissue due to lower scattering and absorption. The ETL lens (Optotune EL-6-18) is placed before the close-coupled scanning mirrors, as close as possible to the conjugate image plane of the back aperture of the miniature objective. By adjusting the focus of the ETL, the focal plane of the microscope is axially scanned within the sample. This obviates the need for an axial scanning mechanism at the distal end of the imaging probe. A 2× beam expander after the scanners forms a light relay between the scanners and the miniature objective,

yielding a 7 mm diameter beam entering the objective lens when the ETL lens is at infinity focal length.

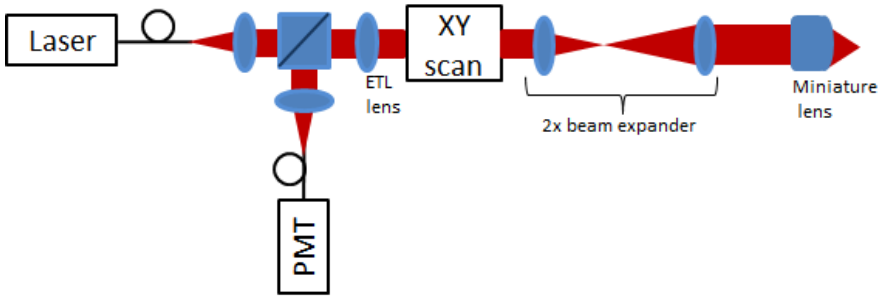

Figure 15: Optical configuration of the RCM system.

Table 7 summarizes the optical specifications of the miniature objective lens, based on the confocal system and the imaging application, and Figure 16 shows the optical layout of the four-element miniature lens imaging system. The objective lens has an effective focal length of 5 mm and a back aperture of 7 mm diameter. The image plane of the objective is allowed to slightly curve to reduce the need for correcting Petzval field curvature which in turn reduces the complexity and size of the objective (e.g. smaller element count). The objective focuses the light to a slightly curved image with 3.3 mm image radius, corresponding to a sag of 6.8 µm, which is less than the thickness of one cell layer within an epithelial tissue sample. The nominal working distance is 305 µm outside the flat last element. The low working distance serves to provide sufficient penetration of light in the tissue and a minimal value to allow the lens to be placed in contact with the sample to reduce motion artifacts during imaging. Because the miniature microscope objective is used in contact with tissue, it is designed to be a water-immersion objective, with a nominal numerical aperture (NA) of 0.7 in

water (n=1.33). The large NA enables the microscope objective to maximize collection of light reflected from the tissue. As the effective focal length of the ETL lens varies from -391 mm to infinity to 60 mm, the light entering the objective lens changes in divergence and beam diameter, resulting in shifts in the working distance and NA of the lens at the tissue space, as reported in Table 8. With 3.75 degrees scan angle entering the objective lens, the paraxial image height equivalent to half field of view (FOV) is 325 μm at the nominal working distance, sufficient for imaging epithelial cells. Table 7 lists the curvatures of all optical surfaces and glass materials of all lenses. Figure 17 shows the performance of the infinity-corrected objective lens at nominal working distance; it shows the field curvature and distortion within the FOV, the RMS wavefront error showing diffraction limited performance across the different fields, and the modulation transfer plots.

Table 7: Optical design specifications of the miniature objective lens

Specification	Value							
Wavelength	811 +/- 5 nm							
Back aperture diameter	7 mm							
Field of view	650 μm dia.							
Plane sag at tissue space	6.8 μm							
Working Distance (μm)	317	303	289	275	259	178	153	41
NA at tissue space	0.7	0.67	0.65	0.62	0.6	0.51	0.48	0.4

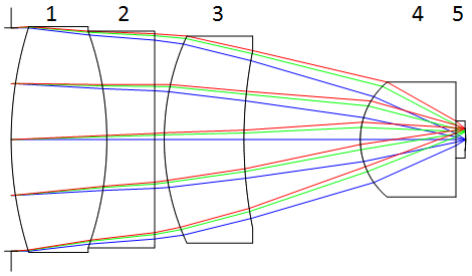

Figure 16: Optical design of the miniature objective lens.

Table 8: Lens system prescription for design in Figure 2. Elements are numbered in ascending order starting from left to right in Figure 2. CX and CC stand for convex and concave respectively.

Element	Radius of curvature		Thickness	Aperture Diameter		Glass
	Front	Back		Front	Back	
Object	Infinity		Infinity			
			Aperture Stop	7 mm		
1	11.458CX	-0.113 CX	3.000	7.0	6.7	NSK14
2	-0.113CC	Infinity	1.500	6.7	6.5	NSF4
			1.378			
3	7.590CX	14.017CC	2.500	6.0	5.1	NLAK12
			3.120			
4	2.352CX	Infinity	3.000	3.2	0.8	NLAK10
5	Infinity	-3.339 CX	0.305	0.8	0.4	'water'
Image	-3.339 CC			0.4		

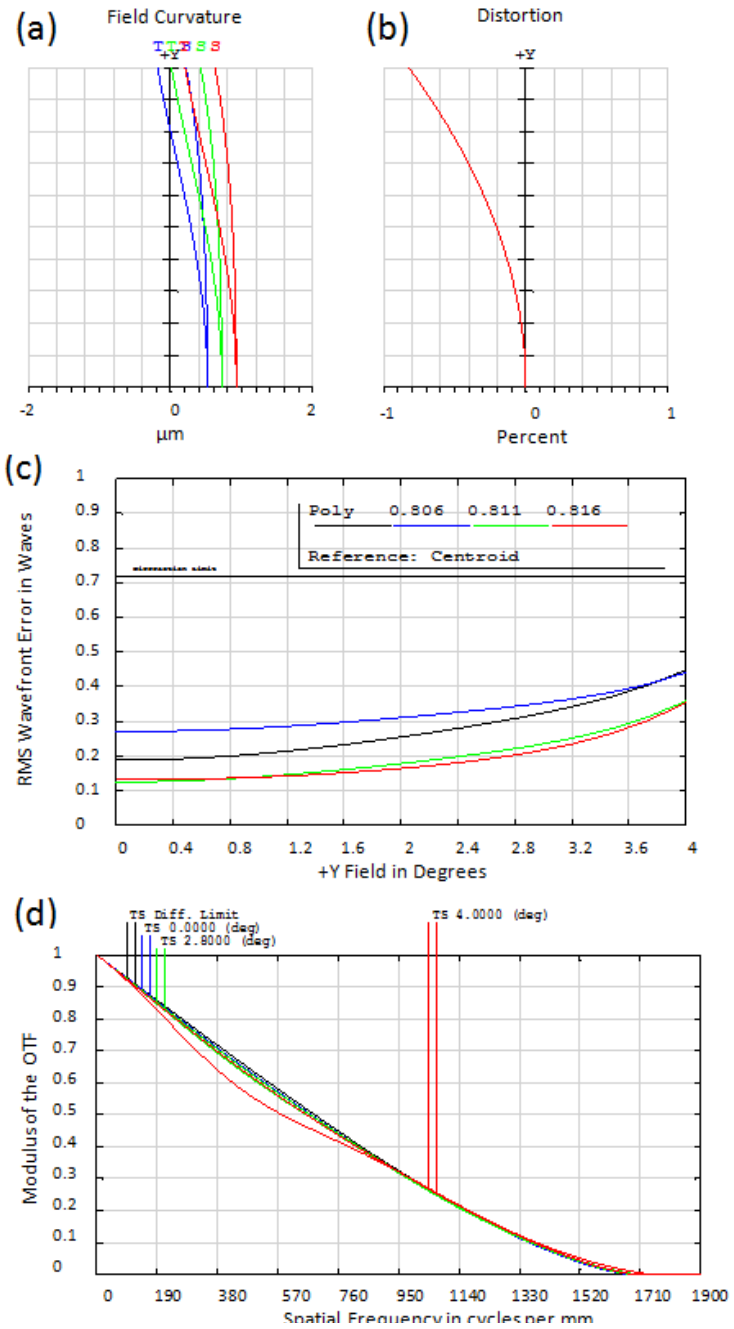

Figure 17: (a) Field curvature and (b) distortion of the miniature objective lens design for wavelengths of 0.806 µm (blue), 0.811 µm (green), and 0.816 µm (red). Maximum field is 4 degrees. (c) RMS wavefront error across field. (d) Polychromatic diffraction modulation transfer function of the miniature objective lens design for the same above fields and for wavelengths from 0.806 to 0.816 µm.

The lens elements were fabricated at Optics Technology Inc., of Rochester, New York with specialty in design and manufacture of lenses with radii of curvature and lens diameters as small as 1 millimeter, coated at Accucoat Inc., and measured for wavefront performance at Metrology Concepts. Optical elements are encased in a stainless steel mechanical housing with black nickel plating. This objective is designed in a smaller format than conventional microscope objectives. The overall length is 20 mm. The barrel outer diameter is 6.5 mm at the surface in contact with tissue, 8.2 mm for the main barrel, and flared to 10 mm at the proximal end. Figure 18 shows photographs of the miniature objective lens. Table 9 lists the fabrication tolerances of the miniature objective lens. The expected as-built performance with this set of tolerances is <0.05 wave root mean square (RMS) for an axial object point and <0.06 wave RMS for a full field object point at 98% yield.

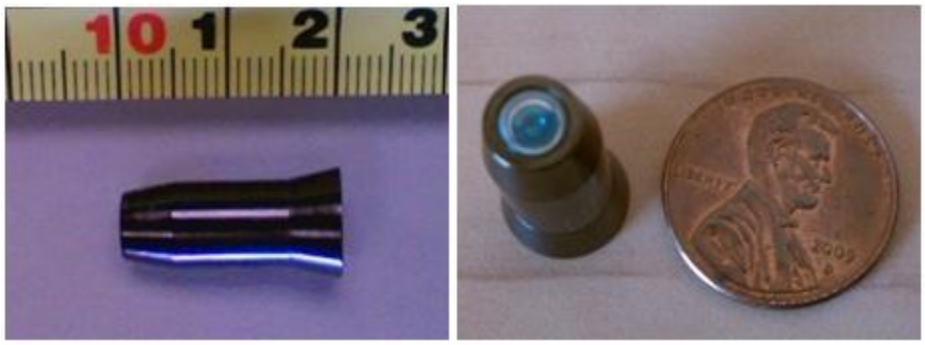

Figure 18: Photographs showing the assembled miniature objective next to a ruler and a United States penny.

Table 9: Lens system tolerances for miniature lens design

Radius (mm)	Thickness/ Airspace (mm)	Irregularity (fringe)	Wedge (mm TIR)	Element Decenter (mm)	Element Tilt (mrad)
±0.025	±0.005 - 0.025	0.25-0.5	0.008 - 0.010	±0.020	±1

The as-built objective lens was evaluated using a Twyman Green interferometer. As shown in Figure 19, the objective lens is illuminated with a collimated wavefront that is retro-reflected back through the objective by means of a high quality reference sphere. The cavity between the objective and retro sphere has a refractive index of 1.33. The interference pattern formed at the beam splitter is imaged onto a camera. The wavefront quality of the miniature objective was assessed by means of phase-shifting, whereby several camera frames of interference fringe patterns are collected after a controlled phase-step of the reference arm by means of a piezo-electric device. In this manner, fringe intensity information is converted to a phase map of the aberrations present in the pupil of the lens under test.

Figure 20 shows the measured on-axis RMS wavefront performance to be 0.042 (well within the 98% yield target of 0.05 wave RMS). The magnitude of wavefront error is often reported in terms of peak to valley (PV) and/or RMS. A practical definition of a "diffraction limited" lens is often considered for lenses with PV results of quarter-wave or RMS results of twentieth of a wave. Although the PV magnitude of wavefront error was measured to be 0.341, the RMS magnitude was 0.042. A RMS metric is often preferred as the more statistically reliable result as it utilizes all available data points; whereas PV relies on just two data points.

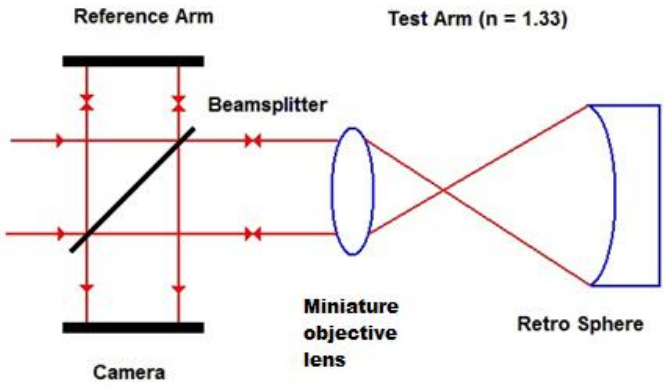

Figure 19: Schematic diagram of the Twyman interferometry setup used for evaluation of the miniature objective lens.

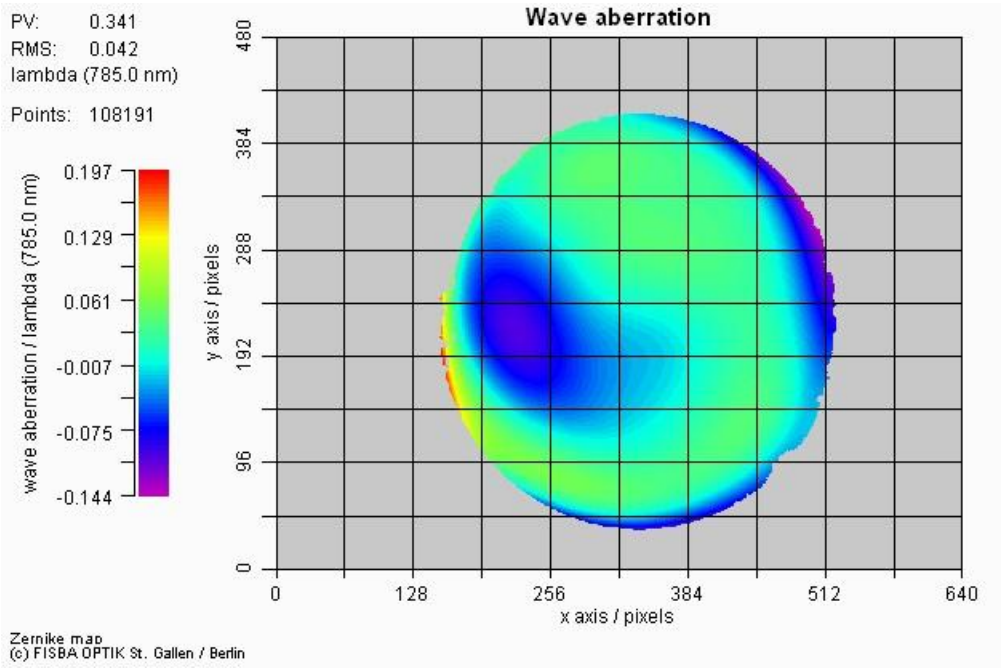

Figure 20: Zernike 2D plot showing the wave aberration of the miniature objective lens

Optical imaging performance of the miniature objective lens was evaluated using the RCM system, shown in Figure 15, using an NIR laser with a center wavelength at 807 nm. To test the axial scan range of the ETL with the miniature lens, a mirror was placed on a motorized stage and the position of best focus was recorded across a range of ETL control current. A total of 200 μm axial scan range was recorded as the control current was varied from 0 to 200 mA. To test the FOV, a Ronchi ruling of 40 line pairs/mm was imaged at the nominal working distance of the lens. A total of 22 line pairs were observed within the FOV which is equivalent to 550 μm across the center of the image (Figure 21(a)). The lateral and axial resolutions were measured across the full range of the control current. Lateral resolution was first evaluated qualitatively by imaging elements of groups 7, 8 and 9 of the standard 1951 U.S. Air Force resolution target. As seen in Figure 21(b), element 6 of group 8 (456.1 line pairs/mm) was clearly resolved. Quantitatively, the lateral resolution was calculated by taking the derivative of the edge-spread function of element 2 of group 6, fitting it to a Gaussian function, and measuring the FWHM of the Gaussian curve as shown in Figure 21(d-f). Axial resolution was measured by translating a planar mirror axially in steps of 0.5 μm and measuring the FWHM of the Gaussian fit of the recorded intensity plot.

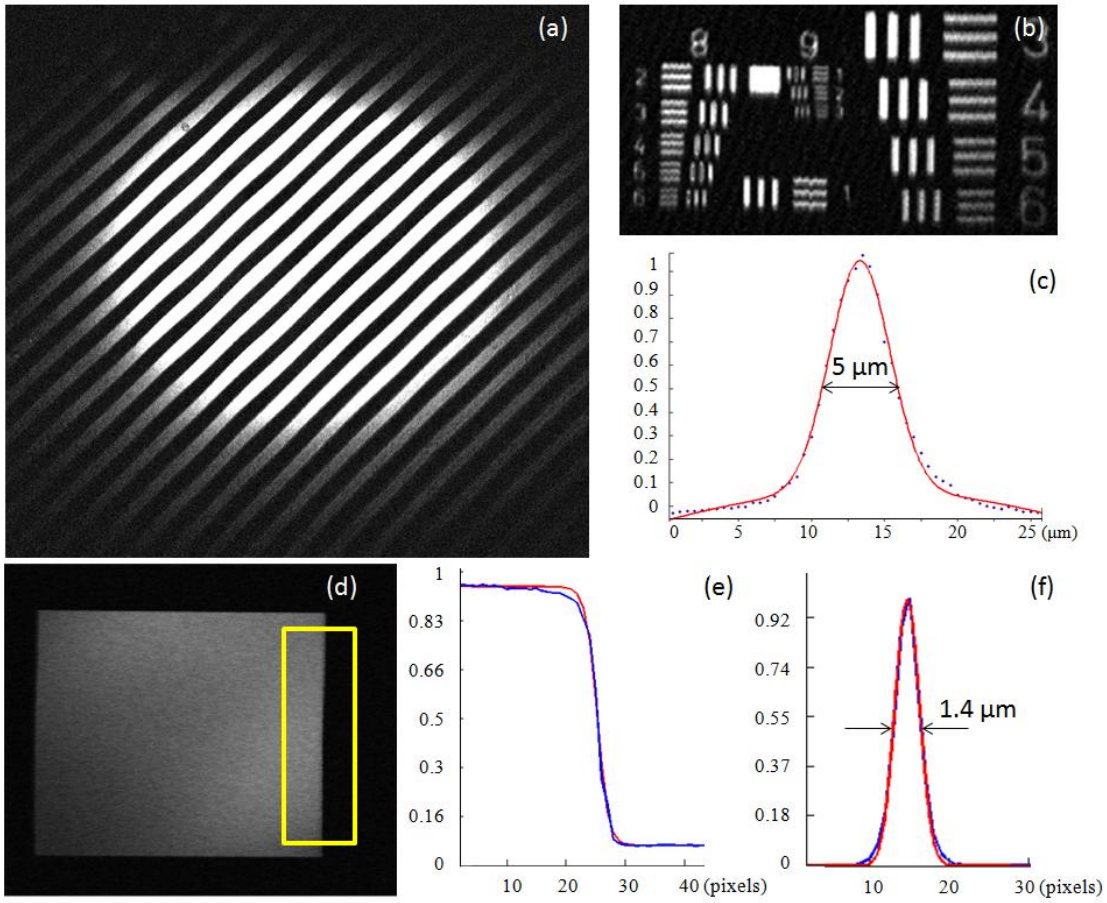

Figure 21: (a) Ronchi ruling showing FOV of the miniature objective lens. (b) Groups 8, 9 and 7 (to the right) of USAF target at 0 mA ETL current. (c) Axial resolution plot showing a FWHM of 5 µm at 0 mA ETL current. (d) Edge used for (e) example of an edge-spread function and its corresponding Boltzmann function fit; (f) point spread function and its corresponding Gaussian function fit with a FWHM of 1.4 µm at 0 mA ETL current.

In order to measure the full optical axial scan range of the system with the ETL, the position of a motorized stage was recorded where a mirror's surface was observed to be in focus as a function of ETL's focal length. Table 10 summarizes these findings along with the corresponding lateral and axial resolution values. The axial resolution varies from 5 µm at the deepest focus to 11 µm close to the surface. This change in

resolution is expected, since as the ETL's focal length varies from infinity to 60 mm, the beam diameter at the back aperture of the objective lens is reduced and therefore the effective NA at the sample decreases. For the purpose of cellular imaging within the epithelium, there is usually less crowding of cells and nuclei at superficial layers, and hence the relatively inferior imaging resolution is acceptable and adequate to resolve the microanatomical features therein. The change in resolution is also dependent on the distance between the ETL and the scanning mirrors; while increasing this distance would result in increased axial range, the extent of telecentricity would decrease resulting in deterioration of the axial resolution. In our case, the lens was positioned as close as possible to the scanning mirrors to preserve telecentricity and to have an acceptable axial resolution change while maintaining a useful axial scan range.

Table 10: Imaging parameters as a function of current applied to the ETL

ETL current (mA)	Axial position of the focus (μm)	Lateral resolution (μm)	Axial resolution (μm)
0	200	1.4	5.0
25	165	1.6	6.0
50	135	1.7	6.7
75	95	1.7	6.9
100	95	1.9	7.5
125	75	1.6	8.0
150	35	1.8	8.7
175	15	1.8	9.0
200	0	1.9	11.0

CHAPTER VI

CLINICAL IMAGING RESULTS

This chapter describes the materials, methods and results from the clinical imaging study performed with the confocal microscope.

The first part describes the ex vivo imaging of normal, inflamed and cancerous human biopsy tissues that were imaged with both stage scan and ETL scan with the system described in chapter IV. This part of the chapter shows confocal images, videos with their corresponding histology images and diagnosis. This section also discusses the morphological differences seen with pre-cancer progression when comparing the different biopsy sample.

The second part describes the in vivo imaging of various oral sites of normal human volunteers that were imaged with the clinical confocal system that uses ETL scan with the miniature custom-objective lens as described in chapter V. This part of the chapter shows in vivo confocal images and videos. For reference to normal histology images from oral tissue, refer to the ex vivo study.

VI.1. Ex vivo imaging

VI.1.A. Materials and methods

The tissue collection and imaging protocols were approved by the Institutional Review Boards at TAMU and Baylor College of Dentistry. Tissue samples were obtained from consenting patients who presented themselves either for osseous surgery or crown lengthening procedures or were suspected to have benign, premalignant or malignant lesions. Upon extraction, the tissue samples were immediately placed in iced phosphate buffered saline solution in order to minimize tissue degradation. Before RCM imaging with the system described in Chapter IV [113]. Imaging was performed within 1 hour following tissue collection. The tissue biopsies were treated with 5% acetic acid for ~60 seconds for contrast enhancement. Biopsies were placed in 10% buffered formalin and processed for H&E histology. The sections were assigned to one of the following categories: normal, benign, mild dysplasia, moderate dysplasia, severe dysplasia or cancer. If any of the sections were found to have more than one disease state, then the most severe diagnosis was assigned to that biopsy.

VI.1.B. Results

Figure 22 shows a comparison of a transverse histological image and *en face* confocal images of a clinically normal gingiva tissue. The confocal images were obtained at different depths within the epithelium of the tissue. Bright nuclei and cell borders on a background of relatively darker cytoplasm can be observed throughout the

thickness of the epithelium. The images from the middle of the epithelium to the basal layer show a noticeable increase in the cell density and N/C ratio – features which compare well with the corresponding regions of the histology section. Such a progression in the pattern of cells is typical of normal oral epithelial tissue as the basal cells divide and mature, and move upward within the epithelium. Video 5 shows a comparison of stage scan versus ETL scan of the ex vivo normal human oral tissue.

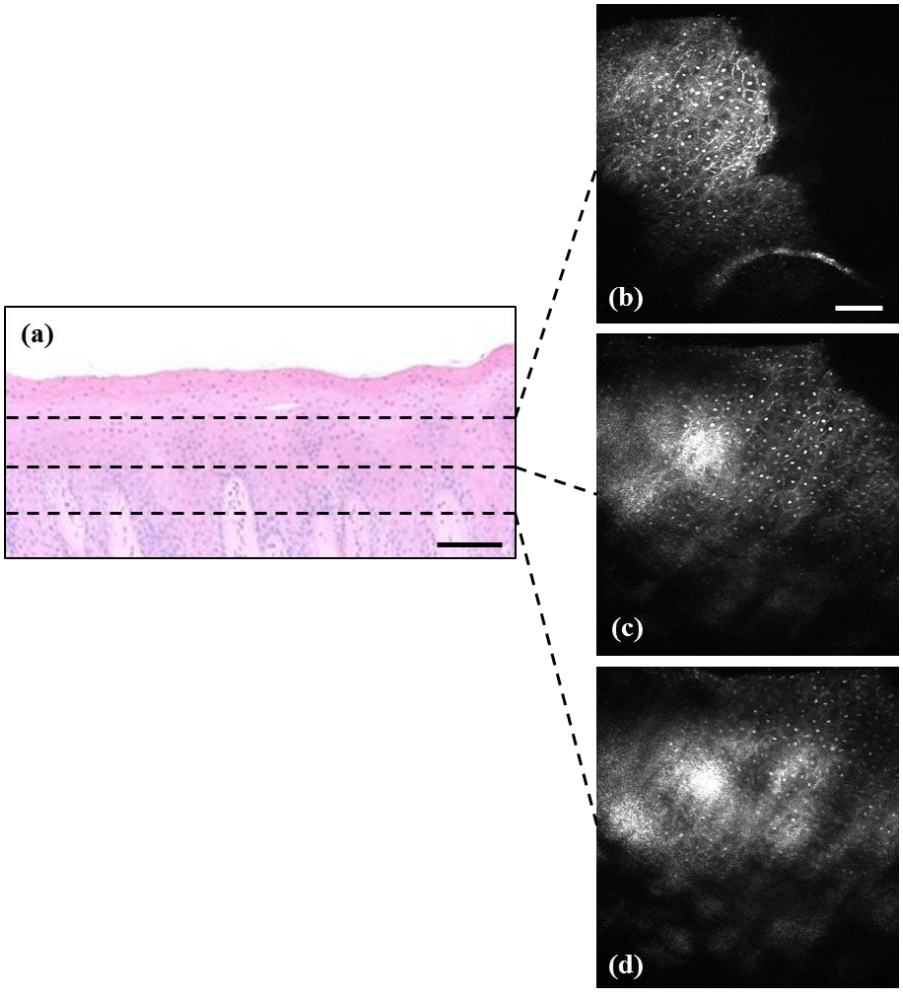

Figure 22: Histology (a) and confocal images (b-d) from different epithelial depths of ex vivo normal human tissue.

Figure 23 shows another set of RCM images taken from a tissue biopsy suspected of inflammation and which was clinically diagnosed as gingival hyperplasia. Again, cell structure could be delineated across the depth of the epithelium. In comparison to the images in Figure 23, there is a marked increase in the proliferation of cells, indicative of hyperplasic growth of the tissue. The peg like structures of rete ridges can also be observed in the images at the interface of the epithelium and lamina propria.

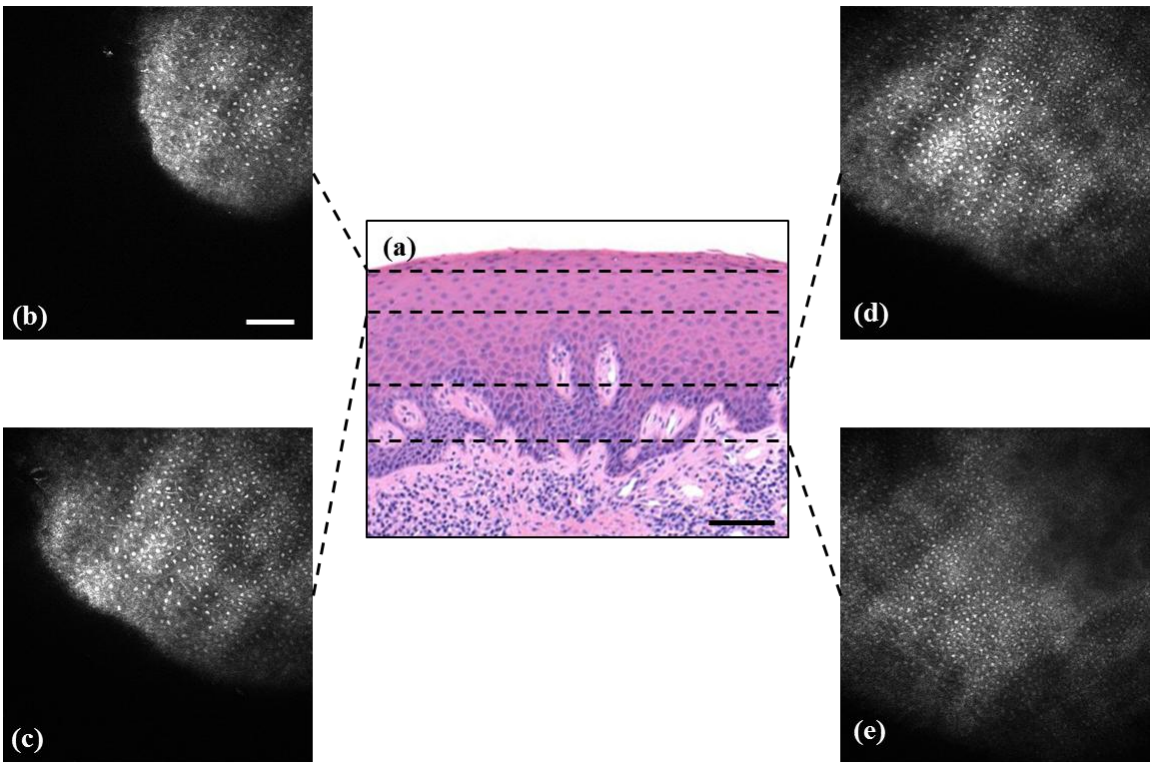

Figure 23: Histology (a) and confocal images (b-e) from different epithelial depths of ex vivo inflamed human tissue.

Figure 24 depicts images from the superficial invasive carcinoma tissue. The region of tissue where confocal images were acquired was interpreted as moderate to

severe dysplasia. The corresponding confocal image mosaic shows an increase in the N/C ratio with increasing depth within the epithelial tissue. The nuclei seen in the RCM images look denser and the abnormal cells appear closer to the surface of the epithelium. Video 6 shows a comparison between normal and SCC ex vivo human oral tissue taken both with ETL scan. Video 7 shows a video of SCC with stage scan.

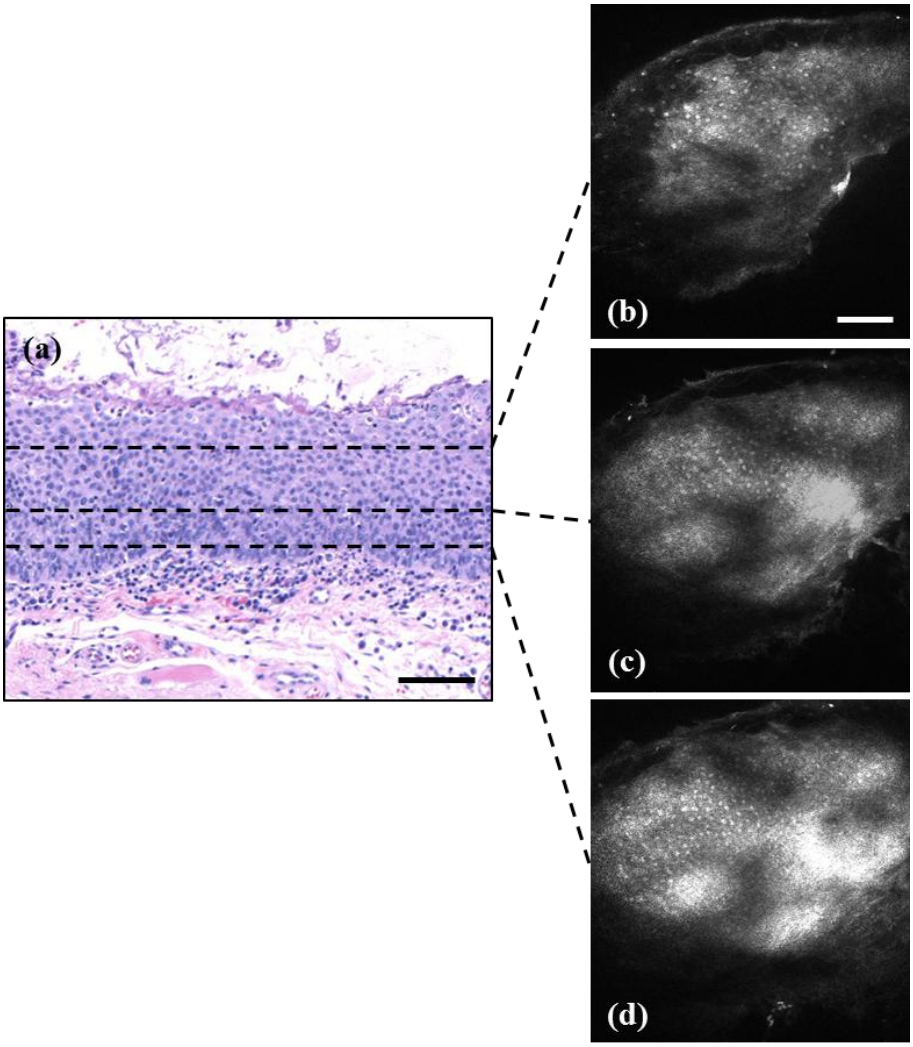

Figure 24: Histology (a) and confocal images (b-d) from different epithelial depths of ex vivo dysplastic human tissue.

This difference of N/C ratio seen in normal tissue from surface to deep becomes less noticeable with the progression of premalignancy as atypical nuclei tend to move up in the epithelium. Similar observation could be made in comparison of nuclear size – the dysplastic tissue exhibits lesser variation in the size while the healthy tissue shows a difference across different depths. The advanced stages of precancer and cancer are characterized by increase in size of the nuclei, and consequently the average distance between the nuclei decreases. Such high concentration of the nuclei can result in decreased scattering of light and, therefore, contrast.

The high resolution microanatomic features seen in RCM allow analysis similar to histological evaluation, wherein the pathologist studies the manifestation of the disease(s) through microscopic examination.

The architectural details can be quantified to more objective parameters (N/C ratio and size of nuclei) which can be directly correlated to that seen in histology. Thickness of the oral epithelium is another feature which can be used to characterize precancerous and cancerous regions within the tissue; however, individuals across different ages, genders, and races can exhibit significant variations in the size of the epithelial thickness [114].

In addition, the thickness of the layer also varies substantially across different regions of the mouth. For instance, the epithelial layer has been measured to be 99 +/- 22 µm thick at the anterior floor of the mouth in comparison to thickness of 294 +/- 68 µm at buccal mucosa [115].

One of the limitations of RCM imaging of is the penetration depth which restricts how deep we can image within the biological tissue. In both our experience and reports by other groups, RCM images have been acquired as deep as ~500 μm in the oral epithelium. While this penetration depth is relatively low in comparison to other imaging modalities such as optical coherence tomography and multi-photon microscopy, most normal values of epithelial thickness within the oral cavity have been noted to be less than 300 μm [115].

More importantly, the areas of the oral cavity most commonly identified with oral cancer are lateral tongue (~200 μm average thickness) and anterior floor of the mouth (~100 μm average thickness), both of which are well within the range of RCM. Nevertheless, the epithelium can show significant increase in thickness during progression of precancer, and potentially limit our ability to image through to the basal cell layer. In addition, regions with severe hyperkeratosis can also reduce the penetration of light due to increased backscattering by the keratin layer.

VI.2. In vivo imaging

VI.2.A. Materials and methods

To demonstrate the practical performance of the miniature objective lens with ETL scanning, imaging of normal human oral mucosa of several volunteers was performed *in vivo*. The protocol was reviewed and approved by the TAMU IRB. Before imaging, a cotton pad soaked in 5% acetic acid was applied to the oral site to be imaged. Acetic acid is applied to increase contrast between the nuclei and the cytoplasm of the epithelial cells in RCM [100]. The tip of the probe was gently placed in contact with the oral tissue to be imaged. The epithelial tissue was scanned with the ETL at scan frequency of 0.2 Hz and an axial scan range of ~200 μm across the ETL control current range of 0 to 200 mA.

VI.2.B. Results

Figure 25 demonstrates the capability of the miniature lens to show sub-cellular epithelial features *in vivo*. Video 8 and Video 9 videos were acquired across the tissue depth of buccal mucosa and inner lip of human volunteers, respectively. Extracted images at multiple depths are shown along with zoomed in images showing features of interest. Bright nuclei (marked by arrows) in contrast with darker cytoplasmic regions could be seen throughout the scanned depth of the tissue. As hypothesized above, while the axial and lateral resolution were inferior in the superficial region of the tissue, the

system was still capable to resolve sub-cellular features, further demonstrating the ability of our RCM embodiment to characterize tissue *in vivo*.

This work shows that our design of a miniature objective lens can successfully enable RCM to image morphological features of the epithelial tissue in *vivo.* The bright nuclei observed across the full depth of the tissues can be utilized to generate more objective parameters such as nuclear size and nuclear-to-cytoplasmic (N/C) ratio, both of which have previously been observed to vary as a function of disease progression in epithelial tissue.

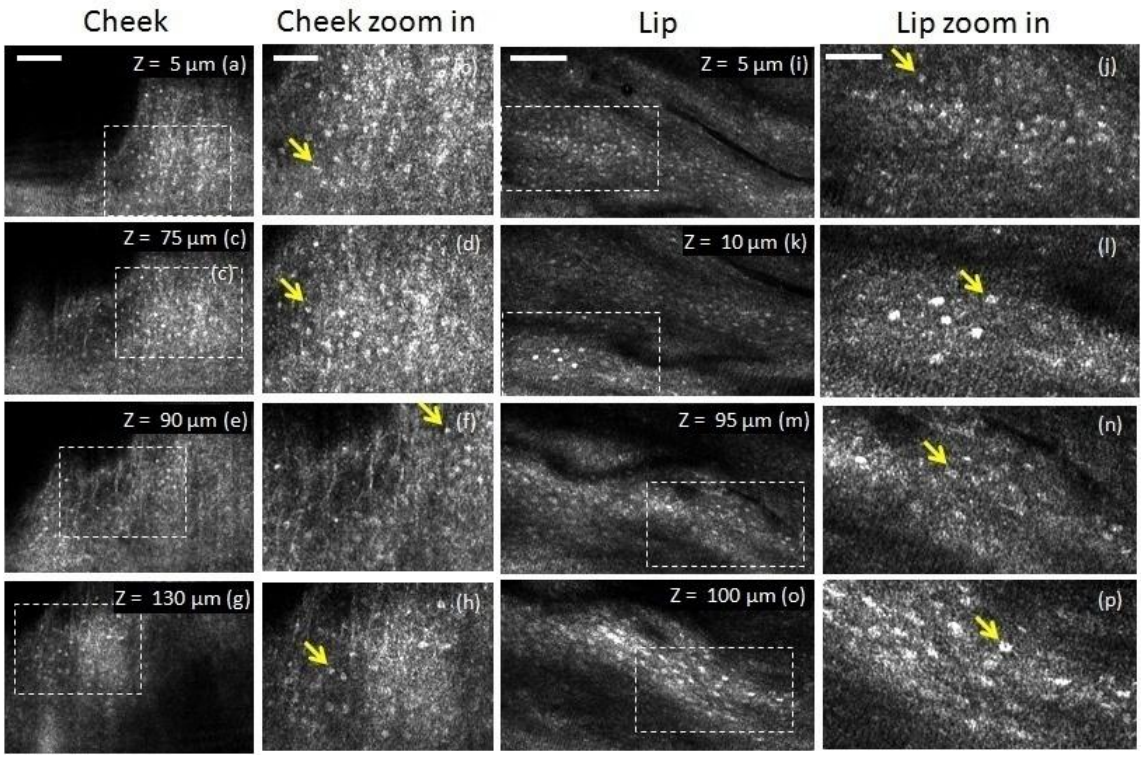

Figure 25: RCM images and videos from human volunteers *in vivo* of (a-h, Video 8) buccal mucosa/cheek and (i-p, Video 9) inner lip tissue. (b, d, f, h) are zoomed in images from the corresponding dashed boxes in (a, c, e, g), and (j, l, n, p) are zoomed in images from the corresponding dashed boxes in (i, k, m, o), respectively. Arrows point to individual nuclei. Cell borders can be seen and identified in (e, f). Scale bars: 100 µm in (a, i) and 50 µm in (b, j) for zoom in versions.

As stated earlier, one of the ultimate goals of this study was to reduce the size of the imaging probe in order to provide better access to biological tissue *in vivo*. The ability to reach internal cavities and regions of the human body is exceedingly critical in order to realize the clinical potential of RCM *in vivo*. Our previous report demonstrating optical axial scanning using a tunable focus lens was a step towards the overall miniaturization of the system, by eliminating the complexity and bulk associated with mechanical scanning. The current study of reducing the size of the objective lens is a further step forward towards fully exploiting the potential of RCM, and we demonstrated the applicability through real-time imaging (Media 1 and Media 2) of multiple locations within the human oral cavity. Our results support the idea that RCM can play a significant role in clinical evaluation of diseased lesions and/or monitoring of tissue response to therapy.

Figure 26 demonstrates the capability of the miniature lens to show in vivo sub cellular epithelial features from different depths of various oral cavity sites of different human volunteers. Bright nuclei are seen along the different depths of the epithelium and are pointed to by yellow arrows. It was observed that various oral mucosa from various oral sites look different in epithelium thickness and clarity of nuclei.

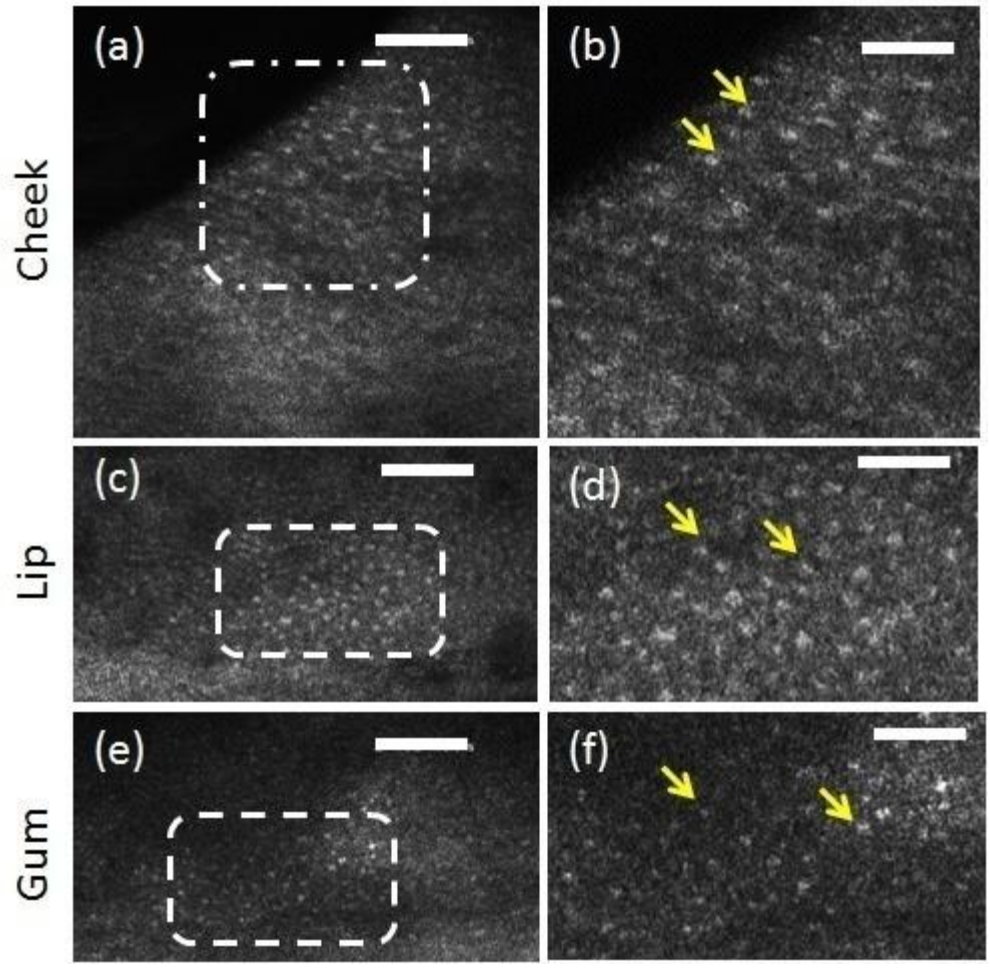

Figure 26: Top: In vivo confocal images of (a,b) cheek, (c,d) lip, and (e-f) gum of different human volunteers. (b, d, f) are zoomed in images from the dashed boxes in (a, c, e) respectively. Scale bars is 125 microns in (a, c, e) and 62.5 microns in (b, d, f).

CHAPTER VII

SUMMARY

In summary, this dissertation has answered three main aims:

1- A multimodal multiscale imaging system was developed and validated. More specifically, RCM was successfully able to differentiate between dysplastic and normal hamster cheek pouch tissue in vivo.

2- An ETL axial scanning mechanism was successfully implemented in an RCM imaging and validated using ex vivo human oral mucosa tissue. A new miniature lens has also been designed and successfully tested for use with ETL axial scanning.

3- The clinical RCM was successfully tested in ex vivo human tissue imaging and in vivo human tissue imaging. Differences between normal, inflamed, precancerous ex vivo human tissue were seen with the RCM system. Normal human oral tissue from different oral sites of different volunteers were imaged and showed sub-cellular resolution epithelial images.

In the future, a quantitative analysis of the RCM images will help for staging the biopsies across the pre-cancer. Moreover, the specificity and the sensitivity need to be assessed by comparison to histopathology. A new side viewing probe is being manufactured to image lesions that are on top of the mouth or the bottom of the mouth below the tongue where the current straight probe cannot access easily.

REFERENCES

1. I. Pavlova, M. Williams, A. El-Naggar, R. Richards-Kortum, and A. Gillenwater, "Understanding the biological basis of autofluorescence imaging for oral cancer detection: High-resolution fluorescence microscopy in viable tissue," Clin Cancer Res **14**, 2396-2404 (2008).

2. P. M. Lane, T. Gilhuly, P. Whitehead, H. S. Zeng, C. F. Poh, S. Ng, P. M. Williams, L. W. Zhang, M. P. Rosin, and C. E. MacAulay, "Simple device for the direct visualization of oral-cavity tissue fluorescence," J Biomed Opt **11**, 0240006-0240001 - 0240006-0240006 (2006).

3. T. Wilson, and A. R. Carlini, "Size of the Detector in Confocal Imaging-Systems," Opt Lett **12**, 227-229 (1987).

4. W. M. Petroll, J. V. Jester, and H. D. Cavanagh, "In vivo confocal imaging: general principles and applications," Scanning **16**, 131-149 (1994).

5. H. D. Cavanagh, W. M. Petroll, and J. V. Jester, "The application of confocal microscopy to the study of living systems," Neurosci Biobehav Rev **17**, 483-498 (1993).

6. C. J. Koester, J. D. Auran, H. D. Rosskothen, G. J. Florakis, and R. B. Tackaberry, "Clinical microscopy of the cornea utilizing optical sectioning and a high-numerical-aperture objective," J Opt Soc Am A **10**, 1670-1679 (1993).

7. P. Corcuff, and J. L. Leveque, "In vivo vision of the human skin with the tandem scanning microscope," Dermatology **186**, 50-54 (1993).

8. M. Rajadhyaksha, M. Grossman, D. Esterowitz, R. H. Webb, and R. R. Anderson, "In vivo confocal scanning laser microscopy of human skin: melanin provides strong contrast," J Invest Dermatol **104**, 946-952 (1995).

9. M. Rajadhyaksha, R. R. Anderson, and R. H. Webb, "Video-rate confocal scanning laser microscope for imaging human tissues in vivo," Appl Opt **38**, 2105-2115 (1999).

10. M. Petran, M. Hadravsky, J. Benes, and A. Boyde, "In vivo microscopy using the tandem scanning microscope," Ann N Y Acad Sci **483**, 440-447 (1986).

11. S. Kimura, and T. Wilson, "Confocal scanning optical microscope using single-mode fiber for signal detection," Appl Opt **30**, 2143-2150 (1991).

12. T. Dabbs, and M. Glass, "Fiber-optic confocal microscope: FOCON," Appl Opt **31**, 3030-3035 (1992).

13. K. Kumar, R. Avritscher, Y. Wang, N. Lane, D. C. Madoff, T. K. Yu, J. W. Uhr, and X. Zhang, "Handheld histology-equivalent sectioning laser-scanning confocal optical microscope for interventional imaging," Biomed Microdevices **12**, 223-233 (2010).

14. R. S. Pillai, D. Lorenser, and D. D. Sampson, "Deep-tissue access with confocal fluorescence microendoscopy through hypodermic needles," Opt Express **19**, 7213-7221 (2011).

15. P. Kim, E. Chung, H. Yamashita, K. E. Hung, A. Mizoguchi, R. Kucherlapati, D. Fukumura, R. K. Jain, and S. H. Yun, "In vivo wide-area cellular imaging by side-view endomicroscopy," Nat Methods **7**, 303-305 (2010).

16. A. F. Gmitro, and D. Aziz, "Confocal microscopy through a fiber-optic imaging bundle," Opt Lett **18**, 565 (1993).

17. B. C. Wilson, "Detection and treatment of dysplasia in Barrett's esophagus: a pivotal challenge in translating biophotonics from bench to bedside," J Biomed Opt **12**, 051401 (2007).

18. E. Laemmel, M. Genet, G. Le Goualher, A. Perchant, J. F. Le Gargasson, and E. Vicaut, "Fibered confocal fluorescence microscopy (Cell-viZio) facilitates extended imaging in the field of microcirculation. A comparison with intravital microscopy," J Vasc Res **41**, 400-411 (2004).

19. B. L. Luck, K. D. Carlson, A. C. Bovik, and R. R. Richards-Kortum, "An image model and segmentation algorithm for reflectance confocal images of in vivo cervical tissue," IEEE Trans Image Process **14**, 1265-1276 (2005).

20. C. Liang, M. Descour, K. B. Sung, and R. Richards-Kortum, "Fiber confocal reflectance microscope (FCRM) for in-vivo imaging," Opt Express **9**, 821-830 (2001).

21. K. B. Sung, C. Liang, M. Descour, T. Collier, M. Follen, A. Malpica, and R. Richards-Kortum, "Near real time in vivo fibre optic confocal microscopy: sub-cellular structure resolved," J Microsc **207**, 137-145 (2002).

22. Y. S. Sabharwal, A. R. Rouse, L. Donaldson, M. F. Hopkins, and A. F. Gmitro, "Slit-scanning confocal microendoscope for high-resolution in vivo imaging," Appl Opt **38**, 7133-7144 (1999).

23. A. R. Rouse, and A. F. Gmitro, "Multispectral imaging with a confocal microendoscope," Opt Lett **25**, 1708-1710 (2000).

24. C. P. Lin, and R. H. Webb, "Fiber-coupled multiplexed confocal microscope," Opt Lett **25**, 954-956 (2000).

25. P. M. Lane, A. L. Dlugan, R. Richards-Kortum, and C. E. Macaulay, "Fiber-optic confocal microscopy using a spatial light modulator," Opt Lett **25**, 1780-1782 (2000).

26. A. J. Thompson, C. Paterson, M. A. Neil, C. Dunsby, and P. M. French, "Adaptive phase compensation for ultracompact laser scanning endomicroscopy," Opt Lett **36**, 1707-1709 (2011).

27. C. Liang, K. B. Sung, R. R. Richards-Kortum, and M. R. Descour, "Design of a high-numerical-aperture miniature microscope objective for an endoscopic fiber confocal reflectance microscope," Appl Opt **41**, 4603-4610 (2002).

28. A. R. Rouse, A. Kano, J. A. Udovich, S. M. Kroto, and A. F. Gmitro, "Design and demonstration of a miniature catheter for a confocal microendoscope," Appl Opt **43**, 5763-5771 (2004).

29. A. A. Tanbakuchi, A. R. Rouse, J. A. Udovich, K. D. Hatch, and A. F. Gmitro, "Clinical confocal microlaparoscope for real-time in vivo optical biopsies," J Biomed Opt **14**, 044030 (2009).

30. K. Carlson, M. Chidley, K. B. Sung, M. Descour, A. Gillenwater, M. Follen, and R. Richards-Kortum, "In vivo fiber-optic confocal reflectance microscope with an injection-molded plastic miniature objective lens," Appl Opt **44**, 1792-1797 (2005).

31. M. D. Chidley, K. D. Carlson, R. R. Richards-Kortum, and M. R. Descour, "Design, assembly, and optical bench testing of a high-numerical-aperture miniature

injection-molded objective for fiber-optic confocal reflectance microscopy," Appl Opt **45**, 2545-2554 (2006).

32. R. T. Kester, T. Christenson, R. R. Kortum, and T. S. Tkaczyk, "Low cost, high performance, self-aligning miniature optical systems," Appl Opt **48**, 3375-3384 (2009).

33. R. T. Kester, T. S. Tkaczyk, M. R. Descour, T. Christenson, and R. Richards-Kortum, "High numerical aperture microendoscope objective for a fiber confocal reflectance microscope," Opt Express **15**, 2409-2420 (2007).

34. K. B. Sung, C. Liang, M. Descour, T. Collier, M. Follen, and R. Richards-Kortum, "Fiber-optic confocal reflectance microscope with miniature objective for in vivo imaging of human tissues," IEEE Trans Biomed Eng **49**, 1168-1172 (2002).

35. R. P. Barretto, B. Messerschmidt, and M. J. Schnitzer, "In vivo fluorescence imaging with high-resolution microlenses," Nat Methods **6**, 511-512 (2009).

36. C. J. Engelbrecht, R. S. Johnston, E. J. Seibel, and F. Helmchen, "Ultra-compact fiber-optic two-photon microscope for functional fluorescence imaging in vivo," Opt Express **16**, 5556-5564 (2008).

37. J. C. Jung, A. D. Mehta, E. Aksay, R. Stepnoski, and M. J. Schnitzer, "In vivo mammalian brain imaging using one- and two-photon fluorescence microendoscopy," J Neurophysiol **92**, 3121-3133 (2004).

38. P. Kim, M. Puoris'haag, D. Cote, C. P. Lin, and S. H. Yun, "In vivo confocal and multiphoton microendoscopy," J Biomed Opt **13**, 010501 (2008).

39. B. A. Flusberg, J. C. Jung, E. D. Cocker, E. P. Anderson, and M. J. Schnitzer, "In vivo brain imaging using a portable 3.9 gram two-photon fluorescence microendoscope," Opt Lett **30**, 2272-2274 (2005).

40. B. Farahati, O. Stachs, F. Prall, J. Stave, R. Guthoff, H. W. Pau, and T. Just, "Rigid confocal endoscopy for in vivo imaging of experimental oral squamous intra-epithelial lesions," J Oral Pathol Med **39**, 318-327 (2010).

41. J. Benschop, and G. van Rosmalen, "Confocal compact scanning optical microscope based on compact disc technology," Appl Opt **30**, 1179-1184 (1991).

42. R. Juskaitis, and T. Wilson, "Direct-view fiber-optic confocal microscope," Opt Lett **19**, 1906 (1994).

43. L. Giniunas, R. Juskaitis, and S. V. Shatalin, "Endoscope with optical sectioning capability," Appl Opt **32**, 2888-2890 (1993).

44. F. Helmchen, M. S. Fee, D. W. Tank, and W. Denk, "A miniature head-mounted two-photon microscope: High-resolution brain imaging in freely moving animals," Neuron **31**, 903-912 (2001).

45. B. H. W. Hendriks, W. C. J. Bierhoff, J. J. L. Horikx, A. E. Desjardins, C. A. Hezemans, G. W. 't Hooft, G. W. Lucassen, and N. Mihajlovic, "High-resolution resonant and nonresonant fiber-scanning confocal microscope," J Biomed Opt **16** (2011).

46. M. T. Myaing, D. J. MacDonald, and X. D. Li, "Fiber-optic scanning two-photon fluorescence endoscope," Opt Lett **31**, 1076-1078 (2006).

47. D. Dickensheets, and G. S. Kino, "A Scanned Optical-Fiber Confocal Microscope," P Soc Photo-Opt Ins **2184**, 39-47 (1994).

48. D. L. Dickensheets, and G. S. Kino, "Micromachined scanning confocal optical microscope," Opt Lett **21**, 764-766 (1996).

49. D. L. Dickensheets, and G. S. Kino, "Silicon-micromachined scanning confocal optical microscope," J Microelectromech S **7**, 38-47 (1998).

50. D. L. Dickensheets, "Requirements of MEMS membrane mirrors for focus adjustment and aberration correction in endoscopic confocal and optical coherence tomography imaging instruments," J Micro-Nanolith Mem **7** (2008).

51. M. J. Moghimi, B. J. Lutzenberger, B. M. Kaylor, and D. L. Dickensheets, "MOEMS deformable mirrors for focus control in vital microscopy," J Micro-Nanolith Mem **10** (2011).

52. K. Murakami, "A miniature confocal optical scanning microscope for endoscope," MOEMS Display and Imaging Systems III **5721**, 119-131 (2005).

53. K. Murakami, A. Murata, T. Suga, H. Kitagawa, Y. Kamiya, M. Kubo, K. Matsumoto, H. Miyajima, and M. Katashiro, "A miniature confocal optical microscope with MEMS gimbal scanner," Boston Transducers'03: Digest of Technical Papers, Vols 1 and 2, 587-590 (2003).

54. K. Kumar, R. Avritscher, Y. M. Wang, N. Lane, D. C. Madoff, T. K. Yu, J. W. Uhr, and X. J. Zhang, "Handheld histology-equivalent sectioning laser-scanning confocal optical microscope for interventional imaging," Biomed Microdevices **12**, 223-233 (2010).

55. K. C. Maitland, H. J. Shin, H. Ra, D. Lee, O. Solgaard, and R. Richards-Kortum, "Single fiber confocal microscope with a two-axis gimbaled MEMS scanner for cellular imaging," Opt Express **14**, 8604-8612 (2006).

56. H. J. Shin, M. C. Pierce, D. Lee, H. Ra, O. Solgaard, and R. Richards-Kortum, "Fiber-optic confocal microscope using a MEMS scanner and miniature objective lens," Opt Express **15**, 9113-9122 (2007).

57. S. P. Poland, L. J. Li, D. Uttamchandani, and J. M. Girkin, "A confocal micro-imaging system incorporating a thermally actuated two axis MEMS scanner," Endoscopic Microscopy Iv **7172** (2009).

58. T. Ota, H. Fukuyama, Y. Ishihara, H. Tanaka, and T. Takamatsu, "In situ fluorescence imaging of organs through compact scanning head for confocal laser microscopy," J Biomed Opt **10** (2005).

59. S. Bargiel, C. Gorecki, T. Verdot, K. Laszczyk, J. Albero, and L. El Fissi, "Electrostatically driven optical Z-axis scanner with thermally bonded glass microlens," Procedia Engineer **5**, 762-765 (2010).

60. T. D. Wang, M. J. Mandella, C. H. Contag, and G. S. Kino, "Dual-axis confocal microscope for high-resolution in vivo imaging," Opt Lett **28**, 414-416 (2003).

61. T. D. Wang, C. H. Contag, M. J. Mandella, N. Y. Chan, and G. S. Kino, "Dual-axes confocal microscopy with post-objective scanning and low-coherence heterodyne detection," Opt Lett **28**, 1915-1917 (2003).

62. J. T. Liu, M. J. Mandella, H. Ra, L. K. Wong, O. Solgaard, G. S. Kino, W. Piyawattanametha, C. H. Contag, and T. D. Wang, "Miniature near-infrared dual-axes

confocal microscope utilizing a two-dimensional microelectromechanical systems scanner," Opt Lett **32**, 256-258 (2007).

63. W. Piyawattanametha, H. Ra, M. J. Mandella, K. Loewke, T. D. Wang, G. S. Kino, O. Solgaard, and C. H. Contag, "3-D Near-Infrared Fluorescence Imaging Using an MEMS-Based Miniature Dual-Axis Confocal Microscope," Ieee J Sel Top Quant **15**, 1344-1350 (2009).

64. H. J. Ra, W. Piyawattanametha, M. J. Mandella, P. L. Hsiung, J. Hardy, T. D. Wang, C. H. Contag, G. S. Kino, and O. Solgaard, "Three-dimensional in vivo imaging by a handheld dual-axes confocal microscope," Opt Express **16**, 7224-7232 (2008).

65. G. J. Tearney, R. H. Webb, and B. E. Bouma, "Spectrally encoded confocal microscopy," Opt Lett **23**, 1152-1154 (1998).

66. G. J. Tearney, M. Shishkov, and B. E. Bouma, "Spectrally encoded miniature endoscopy," Opt Lett **27**, 412-414 (2002).

67. C. Boudoux, S. H. Yun, W. Y. Oh, W. M. White, N. V. Iftimia, M. Shishkov, B. E. Bouma, and G. J. Tearney, "Rapid wavelength-swept spectrally encoded confocal microscopy," Opt Express **13**, 8214-8221 (2005).

68. C. Pitris, B. E. Bouma, M. Shiskov, and G. J. Tearney, "A GRISM-based probe for spectrally encoded confocal microscopy," Opt Express **11**, 120-124 (2003).

69. D. Yelin, C. Boudoux, B. E. Bounia, and G. J. Tearney, "Large area confocal microscopy," Opt Lett **32**, 1102-1104 (2007).

70. A. Osdoit, F. Lacombe, C. Cave, S. Loiseau, and E. Peltier, "To see...the unseeable: Confocal miniprobes for routine microscopic imaging during endoscopy - art. no. 64320F," Endoscopic Microscopy II **6432**, F4320-F4320 (2007).

71. P. M. Delaney, M. R. Harris, and R. G. King, "Fiberoptic Laser-Scanning Confocal Microscope Suitable for Fluorescence Imaging," Appl Opt **33**, 573-577 (1994).

72. P. M. Delaney, R. G. King, J. R. Lambert, and M. R. Harris, "Fiber Optic Confocal Imaging (Foci) for Subsurface Microscopy of the Colon in-Vivo," J Anat **184**, 157-160 (1994).

73. A. L. Polglase, W. J. McLaren, S. A. Skinner, R. Kiesslich, M. F. Neurath, and P. M. Delaney, "A fluorescence confocal endomicroscope for in vivo microscopy of the upper- and the lower-GI tract," Gastrointest Endosc **62**, 686-695 (2005).

74. Y. Kakeji, S. Yamaguchi, D. Yoshida, K. Tanoue, M. Ueda, A. Masunari, T. Utsunomiya, M. Imamura, H. Honda, Y. Maehara, and M. Hashizume, "Development and assessment of morphologic criteria for diagnosing gastric cancer using confocal endomicroscopy: an ex vivo and in vivo study," Endoscopy **38**, 886-890 (2006).

75. R. Kiesslich, J. Burg, M. Vieth, J. Gnaendiger, M. Enders, P. Delaney, A. Polglase, W. McLaren, D. Janell, S. Thomas, B. Nafe, P. R. Galle, and M. F. Neurath, "Confocal laser endoscopy for diagnosing intraepithelial neoplasias and colorectal cancer in vivo," Gastroenterology **127**, 706-713 (2004).

76. S. Kitabatake, Y. Niwa, R. Miyahara, A. Ohashi, T. Matsuura, Y. Iguchi, Y. Shimoyama, T. Nagasaka, O. Maeda, T. Ando, N. Ohmiya, A. Itoh, Y. Hirooka, and H.

Goto, "Confocal endomicroscopy for the diagnosis of gastric cancer in vivo," Endoscopy **38**, 1110-1114 (2006).

77. J. Tan, M. A. Quinn, J. M. Pyman, P. M. Delaney, and W. J. McLaren, "Detection of cervical intraepithelial neoplasia in vivo using confocal endomicroscopy," Bjog-Int J Obstet Gy **116**, 1663-1670 (2009).

78. K. Dunbar, and M. Canto, "Confocal endomicroscopy," Curr Opin Gastroen **24**, 631-637 (2008).

79. G. Le Goualher, A. Perchant, M. Genet, C. Cave, B. Viellerobe, R. Berier, B. Abrat, and N. Ayache, "Towards optical biopsies with an integrated fibered confocal fluorescence microscope," Lect Notes Comput Sc **3217**, 761-768 (2004).

80. B. Viellerobe, A. Osdoit, C. Cave, F. Lacombe, S. Loiseau, and B. Abrat, "Mauna Kea technologies' F400 prototype: a new tool for in vivo microscopic imaging during endoscopy - art. no. 60820C," Endoscopic Microscopy **6082**, C820-C820 (2006).

81. E. Laemmel, M. Genet, G. Le Goualher, A. Perchant, J. F. Le Gargasson, and E. Vicaut, "Fibered confocal fluorescence microscopy (Cell-viZio (TM)) facilitates extended imaging in the field of microcirculation - A comparison with intravital microscopy," J Vasc Res **41**, 400-411 (2004).

82. J. M. Jabbour, M. A. Saldua, J. N. Bixler, and K. C. Maitland, "Confocal Endomicroscopy: Instrumentation and Medical Applications," Ann Biomed Eng **40**, 378-397 (2012).

83. J. Sun, T. Shilagard, B. Bell, M. Motamedi, and G. Vargas, "In vivo multimodal nonlinear optical imaging of mucosal tissue," Opt Express **12**, 2478-2486 (2004).

84. W. M. White, M. Rajadhyaksha, S. Gonzalez, R. L. Fabian, and R. R. Anderson, "Noninvasive imaging of human oral mucosa in vivo by confocal reflectance microscopy," Laryngoscope **109**, 1709-1717 (1999).

85. A. K. Dunn, C. Smithpeter, A. J. Welch, and R. Richards-Kortum, "Sources of contrast in confocal reflectance imaging," Appl Opt **35**, 3441-3446 (1996).

86. K. C. Maitland, A. M. Gillenwater, M. D. Williams, A. K. El-Naggar, M. R. Descour, and R. R. Richards-Kortum, "In vivo imaging of oral neoplasia using a miniaturized fiber optic confocal reflectance microscope," Oral Oncol **44**, 1059-1066 (2008).

87. A. L. Clark, A. Gillenwater, R. Alizadeh-Naderi, A. K. El-Naggar, and R. Richards-Kortum, "Detection and diagnosis of oral neoplasia with an optical coherence microscope," J Biomed Opt **9**, 1271-1280 (2004).

88. J. A. Jo, B. E. Applegate, J. Park, S. Shrestha, P. Pande, I. B. Gimenez-Conti, and J. L. Brandon, "In Vivo Simultaneous Morphological and Biochemical Optical Imaging of Oral Epithelial Cancer," Ieee T Bio-Med Eng **57**, 2596-2599 (2010).

89. Y. C. Ahn, J. R. Chung, P. Wilder-Smith, and Z. P. Chen, "Multimodality approach to optical early detection and mapping of oral neoplasia," J Biomed Opt **16** (2011).

90. M. C. Pierce, R. A. Schwarz, K. Rosbach, D. Roblyer, T. Muldoon, M. D. Williams, A. K. El-Naggar, A. M. Gillenwater, and R. Richards-Kortum, "Wide-field and high-resolution optical imaging for early detection of oral neoplasia," Photonic Therapeutics and Diagnostics Vi **7548** (2010).

91. R. Patel, A. Khan, D. Wirth, M. Kamionek, D. Kandil, R. Quinlan, and A. N. Yaroslavsky, "Multimodal optical imaging for detecting breast cancer," J Biomed Opt **17** (2012).

92. J. B. Epstein, S. Silverman, J. D. Epstein, S. A. Lonky, and M. A. Bride, "Analysis of oral lesion biopsies identified and evaluated by visual examination, chemiluminescence and toluidine blue (vol 44, pg 538, 2008)," Oral Oncol **44**, 615-615 (2008).

93. K. H. Awan, P. R. Morgan, and S. Warnakulasuriya, "Evaluation of an autofluorescence based imaging system (VELscope (TM)) in the detection of oral potentially malignant disorders and benign keratoses," Oral Oncol **47**, 274-277 (2011).

94. M. W. Lingen, J. R. Kalmar, T. Karrison, and P. M. Speight, "Critical evaluation of diagnostic aids for the detection of oral cancer," Oral Oncol **44**, 10-22 (2008).

95. D. C. G. De Veld, M. J. H. Witjes, H. J. C. M. Sterenborg, and J. L. N. Roodenburg, "The status of in vivo autofluorescence spectroscopy and imaging for oral oncology," Oral Oncol **41**, 117-131 (2005).

96. N. P. Galletly, J. McGinty, C. Dunsby, F. Teixeira, J. Requejo-Isidro, I. Munro, D. S. Elson, M. A. A. Neil, A. C. Chu, P. M. W. French, and G. W. Stamp, "Fluorescence lifetime imaging distinguishes basal cell carcinoma from surrounding uninvolved skin," Brit J Dermatol **159**, 152-161 (2008).

97. V. K. Ramanujan, J. H. Zhang, E. Biener, and B. Herman, "Multiphoton fluorescence lifetime contrast in deep tissue imaging: prospects in redox imaging and disease diagnosis," J Biomed Opt **10** (2005).

98. M. C. Skala, K. M. Riching, D. K. Bird, A. Gendron-Fitzpatrick, J. Eickhoff, K. W. Eliceiri, P. J. Keely, and N. Ramanujam, "In vivo multiphoton fluorescence lifetime imaging of protein-bound and free nicotinamide adenine dinucleotide in normal and precancerous epithelia," J Biomed Opt **12** (2007).

99. S. Shrestha, B. E. Applegate, J. Park, X. D. Xiao, P. Pande, and J. A. Jo, "High-speed multispectral fluorescence lifetime imaging implementation for in vivo applications," Opt Lett **35**, 2558-2560 (2010).

100. R. A. Drezek, T. Collier, C. K. Brookner, A. Malpica, R. Lotan, R. R. Richards-Kortum, and M. Follen, "Laser scanning confocal microscopy of cervical tissue before and after application of acetic acid," Am J Obstet Gynecol **182**, 1135-1139 (2000).

101. A. F. Zuluaga, R. Drezek, T. Collier, R. Lotan, M. Follen, and R. Richards-Kortum, "Contrast agents for confocal microscopy: how simple chemicals affect confocal images of normal and cancer cells in suspension," J Biomed Opt **7**, 398-403 (2002).

102. J. M. Jabbour, S. N. Cheng, B. H. Malik, R. Cuenca, J. A. Jo, J. Wright, Y. S. L. Cheng, and K. C. Maitland, "Fluorescence lifetime imaging and reflectance confocal microscopy for multiscale imaging of oral precancer," J Biomed Opt **18** (2013).

103. A. A. Tanbakuchi, A. R. Rouse, J. A. Udovich, K. D. Hatch, and A. F. Gmitro, "Clinical confocal microlaparoscope for real-time in vivo optical biopsies," J Biomed Opt **14** (2009).

104. K. B. Sung, C. N. Liang, M. Descour, T. Collier, M. Follen, and R. Richards-Kortum, "Fiber-optic confocal reflectance microscope with miniature objective for in vivo imaging of human tissues," Ieee T Bio-Med Eng **49**, 1168-1172 (2002).

105. C. Olsovsky, R. Shelton, O. Carrasco-Zevallos, B. E. Applegate, and K. C. Maitland, "Chromatic confocal microscopy for multi-depth imaging of epithelial tissue," Biomed Opt Express **4**, 732-740 (2013).

106. P. M. Lane, R. P. Elliott, and C. E. MacAulay, "Confocal microendoscopy with chromatic sectioning," Spectral Imaging: Instrumentation, Applications, and Analysis Ii **4959**, 23-26 (2003).

107. E. J. Botcherby, R. Juskaitis, M. J. Booth, and T. Wilson, "Aberration-free optical refocusing in high numerical aperture microscopy," Opt Lett **32**, 2007-2009 (2007).

108. B. F. Grewe, F. F. Voigt, M. Van't Hoff, and F. Helmchen, "Fast two-layer two-photon imaging of neuronal cell populations using an electrically tunable lens," Biomed Opt Express **2**, 2035-2046 (2011).

109. F. O. Fahrbach, F. F. Voigt, B. Schmid, F. Helmchen, and J. Huisken, "Rapid 3D light-sheet microscopy with a tunable lens," Opt Express **21**, 21010-21026 (2013).

110. H. S. Chen, and Y. H. Lin, "An endoscopic system adopting a liquid crystal lens with an electrically tunable depth-of-field," Opt Express **21**, 18079-18088 (2013).

111. N. Savidis, G. Peyman, N. Peyghambarian, and J. Schwiegerling, "Nonmechanical zoom system through pressure-controlled tunable fluidic lenses," Appl Opt **52**, 2858-2865 (2013).

112. D. G. Ouzounov, D. R. Rivera, W. W. Webb, J. Bentley, and C. Xu, "Miniature varifocal objective lens for endomicroscopy," Opt Lett **38**, 3103-3106 (2013).

113. J. M. Jabbour, B. H. Malik, C. Olsovsky, R. Cuenca, S. Cheng, J. A. Jo, Y. S. Cheng, J. M. Wright, and K. C. Maitland, "Optical axial scanning in confocal microscopy using an electrically tunable lens," Biomedical optics express **5**, 645-652 (2014).

114. K. L. Vandana, and B. Savitha, "Thickness of gingiva in association with age, gender and dental arch location," Journal of clinical periodontology **32**, 828-830 (2005).

115. S. Prestin, S. I. Rothschild, C. S. Betz, and M. Kraft, "Measurement of epithelial thickness within the oral cavity using optical coherence tomography," Head Neck-J Sci Spec **34**, 1777-1781 (2012).